Faculty of Postgraduate Studies and Scientific Research
German University in Cairo

Development of an Electromagnetic-Based Haptic Interface for Rendering of Volumetric Shapes in Mid-Air

A thesis submitted in partial fulfillment of the requirements for the degree of Master of Science in Mechatronics Engineering

By

Mina Maged Micheal

Supervised by

Dr. Islam S. M. Khalil
Associate Professor

Faculty of Material Science and Engineering
German University in Cairo, New Cairo, Egypt

Department of Biomechanical Engineering
University of Twente, Enschede, The Netherlands

2023

Declaration of Authorship

I, Mina Maged, declare that this thesis titled, "Development of an Electromagnetic-Based Haptic Interface for Rendering of Volumetric Shapes in Mid-Air" and the work presented in it are my own. I confirm that:

- This work was done wholly or mainly while in candidature for a research degree at this University.
- Where any part of this thesis has previously been submitted for a degree or any other qualification at this University or any other institution, this has been clearly stated.
- Where I have consulted the published work of others, this is always clearly attributed.
- Where I have quoted from the work of others, the source is always given. With the exception of such quotations, this thesis is entirely my own work.
- I have acknowledged all main sources of help.
- Where the thesis is based on work done by myself jointly with others, I have made clear exactly what was done by others and what I have contributed myself.

Signed:

Date:

Abstract

Master of Science

Development of an Electromagnetic-Based Haptic Interface for Rendering of Volumetric Shapes in Mid-Air

by Mina Maged Micheal

Mid-Air haptics is an active area of research owing to its potential impact on augmented/virtual reality. In this work, an electromagnetic-based haptic interface (EHI) is developed to generate controlled magnetic forces necessary for rendering three-dimensional (3D) virtual objects in mid-air. A model of the magnetic forces exerted on a dipole attached to a wearable finger splint is developed to optimize the design of the electromagnetic coils. An impedance-type haptic rendering algorithm, utilizing position feedback is designed. This rendering algorithm capitalizes on minimizing the error between the exerted magnetic force and the desired constraint force of a virtual 3D object based on the position of the finger. A magnetic localization system is developed to track the finger of the user within the EHI workspace. The position of the magnetic dipole is estimated using two identical arrays of 3D magnetic field sensors to eliminate the magnetic field generated by the EHI. Measurements acquired using these arrays are used to estimate the position of the magnetic dipole by an artificial neural network (ANN). This network maps the field readings to the position of the magnetic dipole. The proposed magnetic localization system is experimentally validated under four different magnetic fields generated by the EHI. These cases are likely to be encountered during the haptic rendering of virtual shapes. In the absence of the EHI field, the mean absolute position error (MAE) was found to be 0.80 ± 0.30 mm (n = 125). Static and sinusoidal magnetic fields are applied, and the MAEs are 1.26 ± 0.43 mm (n = 125) and 0.91 ± 0.33 mm (n = 125), respectively. A random time-varying magnetic field is applied, and the MAE is 0.86 ± 0.33 mm (n = 125). Our statistical analysis shows that the repeatability of the magnetic localization system is acceptable regardless of the field generated by the EHI, at a 95% confidence level. To investigate the influence of incorporating position feedback and test the ability of the EHI to render virtual objects, we conducted a comparative study for the same group of participants with and without position feedback. Our experimental results show that rendering the virtual objects utilizing position feedback enables participants to achieve a success rate of $66.8 \pm 15\%$ (n = 160) in distinguishing between the geometry of four 3D virtual objects. This rate is decreased to $55.1 \pm 15.8\%$ (n = 160) without position feedback. Statistical analysis shows evidence to conclude that the mean success rate for using position feedback to render virtual objects is greater than rendering objects in the absence of position feedback.

Acknowledgements

First, I would like to express my deepest appreciation and gratitude to my advisor Dr. Islam Khalil for the planning of this work and for his patience, motivation, constant supervision, and immense knowledge, his office door was always open. My sincere gratefulness also goes to my partner and friend Alaaeldine Adel for the great support, for the sleepless nights we were working together before deadlines, and for all the fun we have had throughout the entire process. I warmly thank the MNR lab family, Michael Aziz, Mohaned Mansour, Dalia Mahdy, Youssef Hamed, Barbra Adel, Mahmoud Abdel-Fattah, Ahmed Hassan, Abdallah Mohamed and Mostafa Yasser. We have spent together long days and nights working hard and having fun.

I am also grateful to my father, Maged Micheal for his hi support. Thank you for always having my back. Last but not least, I would like to thank my lovely family, Manal Aziz Gad, Awatef Shehata, Marina Maged, and Mariam Maged for all the unconditional love and support I have been receiving from them since I was a little kid in school and for providing me with unfailing support and continuous encouragement. This accomplishment would not have been possible without them. Thank you.

LIST OF PUBLICATIONS

1. A. Adel, M. M. Micheal, M. Abou Seif, S. Abdennadher, and I. S. M. Khalil, "Rendering of volumetric shapes using an electromagnetic-based haptic system", *The IEEE/RSJ International Conference on Intelligent Robots and Systems (IROS 2018)* , pages 8737-8742 (October 2018).

2. A. Adel, M.Mansour, M. M. Micheal, I. S. M. Khalil and S. Misra, "Magnetic localization for an electromagnetic-based haptic interface", *IEEE Magnetics Letters,* , vol. 10, 2102705 (March 2019).

3. M. M. Micheal, A. Adel, C. -S. Kim, J. -O. Park, S. Misra and I. S. M. Khalil, "2D Magnetic Actuation and Localization of a Surface Milli-Roller in Low Reynolds Numbers,", *IEEE Robotics and Automation Letters,* **vol. 7, no. 2**, pp. 3874-3881 (April 2022).

4. M. Welleweerd, T. Hageman, M. Pichel, D. van As ,H. Keizer ,J. Hendrix, M. M Micheal, I.S.M Khalil, and L. Abelmann, "Performance and application of an open source automated magnetic optical density meter for analyzing magnetotactic bacteria", *Review of Scientific Instruments* , (Accepted).

5. I. S. M. Khalil, A. Adel, D. Mahdy, M. M. Micheal, M. Mansour, N. Hamdi and S. Misra, "Magnetic localization and control of helical robots for clearing superficial blood clots", *APL Bioengineering,* **vol. 3, no. 2, 026104**, May 2019 (Featured Article).

6. M. M. Micheal, A. Adel, and I. S. M. Khalil, "Interaction with Virtual Environments via a Kinesthetic Mid-Air Haptic Device and Augmented Reality", *IEEE World Haptics 2023, Delft, The Netherlands* , (WIP Paper).

7. M. M. Micheal, A. Adel, C. -S. Kim, J. -O. Park, S. Misra and I. S. M. Khalil, "SEMA-A Spherical Electromagnetic Actuator for Rotating Dipole-Field Generation", *IEEE/ASME Transactions on Mechatronics* , (To appear).

Contents

Declaration of Authorship **ii**

Abstract **ii**

Acknowledgements **iv**

List of Figures **viii**

List of Tables **xii**

1 Introduction **1**
1.1 Motivation 1
1.2 Literature Review 2
1.2.1 Robotic-based Kinesthetic Haptic Devices 2
1.2.2 Mid-Air Haptic Devices 2
1.2.3 Magnetic Haptic Devices 3
1.3 Objectives 3
1.4 Thesis Organization 4

2 Electromagnetic-Based Haptic Device **5**
2.1 Magnetic Modeling 5
2.1.1 Magnetic Field and Gradient Control 8
2.2 Electromagnetic Coils Design 10
2.3 Current Control Unit 11

3 Localization system **13**
3.1 Optical Localization System 13
3.2 Magnetic Localization System 14
3.2.1 Magnetic Localization System Description 15
3.2.2 Localization Algorithm 15
3.2.3 Magnetic Tracking Validation 17

4 Haptic Rendering **20**
4.1 Magnetic Haptic Rendering Algorithm 20
4.1.1 Constraint Surface Forces 21
4.1.2 Magnetic Forces 24
4.1.3 Current Control Algorithm 25
4.2 Magnetic Rendering Validation 26

4.2.1 Magnetic Rendering of a Virtual Flat Surface 26
4.2.2 Magnetic Rendering of a Virtual Hemisphere 27
4.3 Participant Study and Statistical Analysis 27
4.4 Integration of Magnetic Rendering and Augmented Reality 32
4.5 Challenges and Discussions 34

5 Conclusions and Future Work **36**
5.1 Conclusions 36
5.2 Future Work 36

A Background **38**
A.1 Magnetostatics 38
A.1.1 Maxwell's Equations 38
A.1.2 Magnetostatics 39
A.2 Magnetic Field calculation 39
A.2.1 Magnetic Field off the Symmetry Axis of a Current Loop 39
A.2.2 Magnetic Field Due to Multi-layers Circular Turns Solenoid 41
A.2.3 Magnetic Field Due to a Cylindrical Ferromagnetic Core 41

Bibliography **43**

List of Figures

2.1 Haptic magnetic rendering of virtual objects in mid-air enables a participant to distinguish the features of three-dimensional (3D) virtual objects. The magnetic rendering is achieved using an electromagnetic-based haptic interface. This interface consists of an array of electromagnetic coils, a wearable orthopedic finger splint with a single magnetic dipole moment, and an impendence-type haptic rendering algorithm. Each coil is powered independently using a current source. A current input ($\mathbf{I} \in \mathbf{R}^{9\times1}$) is provided to the coils based on the geometry of the object and the position ($\mathbf{p} \in \mathbf{R}^{3\times1}$) of the user. The system exerts a controlled magnetic force based on the geometry of the 3D virtual objects and observations of participants are used to evaluate the system. 6

2.2 An electromagnetic-based haptic interface enables the operator to interact with virtual objects in three-dimensional (3D) space. (a) A position-sensing device is used to measure the position of the wearable finger splint in 3D space. (b) The position of the wearable finger splint is fed back to the control system to exert a magnetic force based on the rendered geometry. (c) Magnetic rendering of the half-sphere is achieved and participants distinguish its features with a success rate of 67.5%. (d) Participants distinguished this geometry in 65 seconds. 11

3.1 Localization system is developed for an EHI. 14

3.2 Localization system is developed for an EHI. Schematic representation shows a magnetic dipole (1) and a planar configuration of electromagnetic coils (2). The magnetic localization system consists of two identical arrays of 3D magnetic field sensors. The first (3) and second (4) arrays are fixed above and below the EHI, respectively. 15

3.3 Magnetic localization algorithm. The magnetic field measurements are acquired from both the upper and the lower sensors array, the magnetic field due to the EHI is eliminated by subtracting the magnetic field measurements of the upper array from that of the lower array. The magnetic field sensor measures the maximum value after subtraction in selected and fed to an artificial neural network (ANN) to estimate the position of the finger magnet. . . 16

3.4 Histogram of the residual mean position error for the trained neural network is calculated with a coefficient of determination of 0.999. 17

3.5 Magnetic localization system is experimentally validated. (a) Results of the estimated position using S_i sensors under the absence $\hat{R}_1$ and the presence $\hat{R}_2$ of the magnetic field generated by the EHI for 25 different reference points R and a predefined path $\mathbf{p_d}$ in a two-dimensional validation board. This test is performed under four different cases of the field generated by the EHI. Zero (Case 1), static (Case 2), sinusoidal (Case 3), and time-varying magnetic field (Case 4). $\hat{\mathbf{p}}_{d1}, \hat{\mathbf{p}}_{d2}, \hat{\mathbf{p}}_{d3}$, and $\hat{\mathbf{p}}_{d4}$ are the estimated paths for Cases 1-4, respectively. (b) Resultant magnetic field generated by the magnetic dipole and the EHI during Case 2 for the ith sensor. (c) Resultant magnetic fields generated by the magnetic dipole and the EHI are measured in Case 3 for the ith sensor. 18

3.6 Accuracy and the repeatability of the magnetic localization system are experimentally investigated for Cases 1-4, respectively. Our statistical analysis shows that the repeatability of the localization system is acceptable, at $\alpha = 0.05$ and 95% confidence level. 19

4.1 An electromagnetic-based haptic interface enables the operator to interact with virtual objects in mid-air. A position sensing device is used to measure the position of the wearable finger splint in 3D space. Position of the wearable finger splint is fed back to an impedance-type haptic rendering algorithm to exert a magnetic force based on the rendered three-dimensional (3D) virtual object geometry(flat, half-sphere, half-cylinder, and wedge). 21

4.2 Magnetic Rendering Algorithm. 22

4.3 The constraint surface $g(r,t)$ of the virtual object (blue curve) provides a constraint force $g(r,t)$. Magnetic field $B(p)$ at a point p exerts a magnetic force on the magnetic dipole $\mathbf{m}$. This magnetic dipole is attached to the operator via an orthopedic finger splint, and its position is measured using a position localization system. The variables R_i, R_o, and L_c represent the inner-diameter, outer-diameter, and length of the coil, respectively. Note that $\mathbf{r}$ is the position of a point on the constraint surface 23

4.4 Three-dimensional model of a heart is modeled and programmed into a head-mounted display. The boundaries of the heart are magnetically rendered to enable participants to interact with its surface. (a) A model of the heart is generated and its upper half is extracted. (b) A point cloud is generated for the heart. (c) Each point is mapped into a constraint force that is greater than the sensory range of humans. (d) The trajectories taken during interaction with the virtual heart indicate that the operator slides one finger on its boundaries using visual and force feedback 24

4.5 A representative magnetic rendering of a flat surface (at a height of 50 mm) shows the position of the operator and the calculated forces and currents during shape differentiation. (a) The constraint $(g(r,t))$ of the flat surface is decomposed into 3721 points (small black circles). The trajectory of the finger splint indicates a deviation from the rendered flat surface only outside the workspace of the system. (b) The position of the finger splint along the z-axis indicates a maximum deviation of 14 mm from the flat surface during this trial. At the time, $t = 6$ second, the participant moves outside the workspace of the system. (c) Current inputs are calculated and supplied to the electromagnetic coils based on the position of the wearable finger split during this trial. (d) The participant slides his finger on the surface several times. The successful participants differentiate the virtual flat surface from other objects in 92 seconds. 26

4.6 A representative magnetic rendering of a virtual half-sphere (with diameter of 100 mm) shows the position of the operator and the calculated forces and currents during shape differentiation. (a) The constraint surface of the flat surface is decomposed into 3721 points (small black circles). The trajectory of the finger splint indicates that the participant approaches towards the virtual sphere and move along its constraint surface. (b) Notable deviations between position of the participant along z-axis are observed only outside the virtual sphere owing to the absence of controlled magnetic forces. (c) Current inputs are calculated and supplied to the electromagnetic coils based on the position of the wearable finger split during this trial. (d) The participant slides his finger on the surface several times. The successful participants differentiate the virtual flat surface from other objects in 68 seconds. 28

4.7 The observations of five representative participants indicate their ability to differentiate between four virtual shapes (flat, half-sphere, half-cylinder, and wedge). Each participant is allowed to distinguish between the objects for 16 trials only. Our system renders the objects in a random order and the result of each observation is not provided to the participant after each trial. (a) The filled and empty markers indicate the successful and unsuccessful trials, respectively. (b) Participants spent a relatively short time in making successful observations for the virtual sphere and wedge, as opposed to the virtual flat surface and half-cylinder. 30

4.8 The ability of the participants to distinguish between the virtual geometries is enhanced by the incorporation of position feedback. (a) Measurements are collected from the observation of 10 participants using position feedback (Case I) and without (Case II) position feedback. (b) The impedance-type haptic interface enables participants to distinguish objects with 66.87% success rate, whereas exploring the virtual objects without position feedback achieves success rate of 55.15%. The means and standard deviations are calculated using 16 trials for each of the 10 participants in each case. 32

4.9 integration of magnetic rendering and AR enables a participant to interact with virtual objects. Visual feedback is provided via a head-mounted display. The constraint surface of the object is rendered using magnetic forces. These forces are exerted on a wearable orthopedic finger splint using an EHI. A virtual organ (heart) is deployed within the workspace of the electromagnetic system. 34

A.1 Off-axis magnetic field generated by a cylindrical ferromagnetic core 41

List of Tables

4.1 EXPERIMENTAL RESULTS OF THE MAGNETIC RENDERING OF FOUR REPRESENTATIVE THREE-DIMENSIONAL (3D) VIRTUAL OBJECTS, I,E., FLAT SURFACE, HALF-SPHERE, HALF-CYLINDER, AND WEDGE. FIVE PARTICIPANTS EXPERIMENTALLY DEMONSTRATE $66.9 \pm 15.0\%$ SUCCESS RATE ($n = 160$) IN DISTINGUISHING THE FOUR 3D GEOMETRIES USING THE IMPEDANCE-TYPE HAPTIC RENDERING ALGORITHM. IN THE ABSENCE OF POSITION FEEDBACK, THE SUCCESS RATE IS $55.15 \pm 15.80\%$. 29

4.2 EXPERIMENTAL RESULTS OF THE MAGNETIC RENDERING OF FOUR REPRESENTATIVE THREE-DIMENSIONAL (3D) VIRTUAL OBJECTS, I.E. FLAT SURFACE, HALF-SPHERE, HALF-CYLINDER, AND WEDGE. FIVE PARTICIPANTS EXPERIMENTALLY DEMONSTRATE $66.87 \pm 15.0\%$ SUCCESS RATE ($n = 160$) IN DISTINGUISHING THE FOUR 3D GEOMETRIES USING THE IMPEDANCE-TYPE HAPTIC RENDERING ALGORITHM. IN THE ABSENCE OF POSITION FEEDBACK (BETWEEN BRACKETS), THE SUCCESS RATE IS $55.15 \pm 15.8\%$. 31

4.3 CONFUSION MATRIX SHOWS THE PREDICTED OBJECTS (ROW) VERSUS THE ACTUAL OBJECTS (COLUMN) FOR THE IMPEDANCE-TYPE HAPTIC INTERFACE ($n = 160$) AND FOR RENDERING VIRTUAL OBJECTS WITHOUT POSITION FEEDBACK ($n = 160$). MEASUREMENTS OF THE SECOND CASE IS SHOWN BETWEEN BRACKETS. 33

Chapter 1

Introduction

1.1 Motivation

There has been considerable progress in the field of augmented/virtual reality (AR/VR) technologies owing to their potential in several applications such as medical simulation training, education, and the video game industry (Otaduy and Lin, 2005). Virtual and augmented reality technologies allow synthetic computer-generated content to be superimposed onto the real world delivering immersive visualization of virtual content in a mixed-reality environment. This technology gained immense popularity in recent years owing to its various applications ranging from entertainment, education, and manufacturing to training simulators and has become increasingly relevant to the medical and surgical field [Bermejo and Hui, 2017a]. A basic feature for any of these applications is to provide the operator with the ability to interact and explore virtual objects with minimal contact and interaction. However, augmented reality lacks realism and expressively compared to traditional physical means which involves the human sense of touch.

When interacting with real-world objects humans receive a rich stream of tactile information. This information enables us to perceive the objects using our sense of touch with near to 100% accuracy (Martinez et al., 2019). Our human nervous system is responsible for the two primary types of sensation: kinesthetic and cutaneous. Kinesthetic systems employ receptors located in our muscles, tendons, and joints for the sensing of forces and displacements. When holding an object in your hand, kinesthetic feedback tells your brain the approximate size, weight, and orientation of the object relative to your body i.e. it gives the physical world around us the right dimension. Cutaneous or tactile feedback is responsible for stimulating the receptors located on the skin to feel vibrations, pressure, temperature, and the texture of any object [Hannaford and Okamura, 2016]. The science of experiencing and creating touch sensations in human operators is called Haptics. The term 'haptic' is from the Greek word 'haptesthai', meaning 'to touch', and is used to describe something relating to or based on the sense of touch.

A major example driving much of today's haptic virtual environment research is medical training simulators which gained much research attention as an alternative solution for the traditional training methods used in medical schools including tissue phantoms, animals, and corpses [Coles, Meglan, and John, 2011] and [Li et al., 2014]. Incorporating haptic technology into Virtual/Augmented reality medical simulators plays a crucial role in enhancing training realism in procedures such as stitching, needle insertion, endoscopy, laparoscopy,

and palpation [Escobar-Castillejos et al., 2016]. For instance, surgeons manually palpate the area of interest with their fingers during normal medical assessments or open surgeries to detect abnormalities or tumors using their sense of touch, as tissues with possible tumors are stiffer than those of the surroundings. Surgeons could be trained to distinguish between healthy tissues and tumors by perceiving their stiffness using the haptic interface while wearing the AR headset.

1.2 Literature Review

1.2.1 Robotic-based Kinesthetic Haptic Devices

Numerous research groups have utilized robotic-based kinesthetic haptic devices in several applications such as medical simulation training, education, and the entertainment industry. The most widely used haptic devices are Touch™, Phantom®Premium™ from 3D Systems Inc., and Falcon from Novint Technologies Inc. For instance, several researchers developed haptic palpation simulators. Ullrich and Kuhlen [Ullrich and Kuhlen, 2012] used two Touch™ devices (formerly Phantom Omni) to develop a medical simulator to help doctors in palpation during surgeries, They modified the end-effector of the device by adding a lightweight pad for more realistic palpation tasks. Participant study results showed an average acceptance of the simulator performance, however, they reported that the pad modification is a strong improvement over the default stylus. Palmerius *et al.* [Palmerius et al., 2011] have introduced the method of acquiring haptic palpation data from a stiffness map constructed through an elastic imaging modality known as elastography. The authors adopted a Touch X™ device for the haptic feedback in their prototype implementation. Mechanical haptic devices used in the suffer from inherent inner friction, a certain degree of inertia as well as limited workspace the device stylus provides which is inadequate for medical haptic rendering.

1.2.2 Mid-Air Haptic Devices

Mid-air haptics is an emerging technology that can enhance interaction in virtual environments by providing haptic perception in mid-air. This technology aims to convey haptic stimuli at a distance without -in any way- instrumenting the user. Therefore, midair devices are more suitable for AR/VR ecosystems [Bermejo and Hui, 2017b]. Several research groups have developed mid-air haptic devices based on forces generated at a distance using acoustic radiation pressure [Iwamoto et al., 2008], and air pressure [Suzuki and Kobayashi, 2005]. Hoshi *et al.* have integrated visual feedback and force sensing using a hologram and four ultrasonic transducers, respectively [Hoshi, Abe, and Shinoda, 2009]. Long *et al.* have also developed an ultrasound-based haptic feedback method with an array of ultrasonic transducers [Long et al., 2014a]. Spelmezan *et al.* have developed a wearable ultrasound-based haptic device using an array of transducers attached to the user's hand [Spelmezan, González, and Subramanian, 2016]. The usefulness of the ultrasound-based technique is limited by the following two major drawbacks [Arafsha et al., 2015]: first, the generated

force is relatively low (less than 29 mN), and hence its capability to render deformable bodies is limited; second, ultrasound waves require relatively high power (approximately 100 mW/cm2 to exert force of 428 mN) that can cause negative side-effects to skin tissue. Sodhi *et al*. have proposed a mid-air haptic device based on an air-jet technique. This method enables the user to perceive the air pressure as a force [Sodhi et al., 2013]. Suzuki et al. have proposed a force feedback technique based on air pressure for rendering volumetric shapes in mid-air [Suzuki and Kobayashi, 2005]. A combination of laser- and ultrasonic-based approaches have been proposed by Lee et al., 2016 and Ochiai et al., 2016. These air-jet systems have some disadvantages such as their low spatial resolution, relatively large size, and relatively slow response [Arafsha et al., 2015], [Brink et al., 2014]. These problems can be partially overcome by rendering volumetric shapes using computer-controlled magnetic forces on a magnetic dipole [Zhang, Dong, and El Saddik, 2016].

1.2.3 Magnetic Haptic Devices

In recent years, electromagnetic-based haptic interfaces (EHIs) have obtained considerable attention due to their effectiveness in medical simulation applications [Hu et al., 2006]. The EHIs are classified into two groups: Lorentz-forces interfaces [Berkelman, Butler, and Hollis, 1996], [Berkelman and Hollis, 2000], [Salcudean and Vlaar, 1997] and untethered interfaces [Berkelman, Miyasaka, and Anderson, 2012] and [Berkelman, Bozlee, and Miyasaka, 2013]; the latter is achieved using two methods: first, a stylus-based type where the haptic sensation is achieved via a magnetic force exerted on the dipole of an interaction stylus [Tong et al., 2018] and second, a wearable-based type where the magnetic dipole is attached to a wearable device [Zhang, Dong, and El Saddik, 2016]. The second type produces static magnetic forces regardless of the position of the operator. The magnetic force and torque exerted on a dipole can be precisely controlled to render three-dimensional (3D) virtual objects. Zhang *et al*. have proposed a magnetic system for rendering volumetric shapes in mid-air. They have designed and simulated the rendering process of virtual shapes using the magnetic forces exerted on a magnetic dipole without position feedback [Zhang, Dong, and El Saddik, 2016]. Adel *et al*, have demonstrated the ability to generate controlled magnetic forces on a wearable haptic device (wearable orthopedic finger splint) without position feedback [Adel et al., 2017]. The implication of using this technique is that it requires a relatively large number of coils to render all features of complex objects. Moreover. any movement away from a pre-defined constraint surface of the 3D virtual object would decrease the ability of the operator to perceive its features, and as a consequence, the ability of the participants to distinguish between different geometries has not been statistically significant [Adel et al., 2018].

1.3 Objectives

In this thesis, an electromagnetic-based haptic device is developed for rendering 3D virtual objects. An impedance-type haptic rendering algorithm using position feedback is designed

and achieves the following:

- Modeling of the force exerted on a dipole under the influence of a controlled external magnetic field.
- Optimization of the parameters of the electromagnetic coils to obtain force in excess of 2 N at a height of 3 cm
- Development of a magnetic localization system that does not depend on the pre-calculated magnetic field map of the EHI.
- Development of an impedance-type haptic rendering algorithm for rendering 3D virtual objects.
- Experimental investigation on the ability of participants to differentiate between 3D virtual objects.

1.4 Thesis Organization

The remainder of this thesis is organized as follows; Chapter 2 provides modeling of the magnetic force exerted on a dipole attached to a finger splint and the design of an electromagnetic haptic interface. The finger localization system and the localization algorithm are presented in Chapter 3. Chapter 4 presents the haptic rendering algorithm and the experimental investigation of the ability of the participants to differentiate between 3D virtual objects. Finally, Chapter 5 concludes the work and provides future directions.

Chapter 2

Electromagnetic-Based Haptic Device

The electromagnetic haptic device should be able to provide magnetic forces for rendering the required shape on the user's fingertip at any position within its workspace. The electromagnetic-based haptic device consists of four fundamental hardware components

- An array of nine electromagnetic coils
- Wearable user interface
- Hand-tracking system
- Current control unit

The electromagnetic coils are used to provide controlled magnetic forces on a wearable user interface with a single embedded permanent magnet. The position of the user's finger is continuously tracked to determine the required surface constrain forces needed to render a shape. An impedance-type haptic rendering algorithm -which will be presented later- provides control signals via the current control unit to the electromagnetic coils which maps the signals from the algorithm into magnetic forces. These forces render a 3D virtual environment for an operator to perceive.

2.1 Magnetic Modeling

Magnetic haptic rendering of 3D virtual objects is achieved by applying magnetic forces to a single dipole moment ($\mathbf{m} \in \mathbf{R}^{3\times1}$) attached to a wearable finger splint. The objective is to design an electromagnetic-based haptic device capable of generating the necessary magnetic fields $\mathbf{B}(\mathbf{p}) \in \mathbf{R}^{3\times1}$ and field gradients to deliver controlled magnetic forces for haptic feedback. To accomplish this, it is essential to model the magnetic force acting on a single dipole moment when it is exposed to a controlled magnetic field. Let $\mathbf{p} \in \mathbf{R}^{3\times1}$ be the position of the permanent magnet attached to the finger splint. If a controlled magnetic field is applied using a configuration of a planar array of n-electromagnetic coils then a magnetic force ($\mathbf{F} \in \mathbf{R}^{3\times1}$) is generated and is given by

$$\mathbf{F} = \nabla(\mathbf{B}(\mathbf{p}) \cdot \mathbf{m}), \tag{2.1}$$

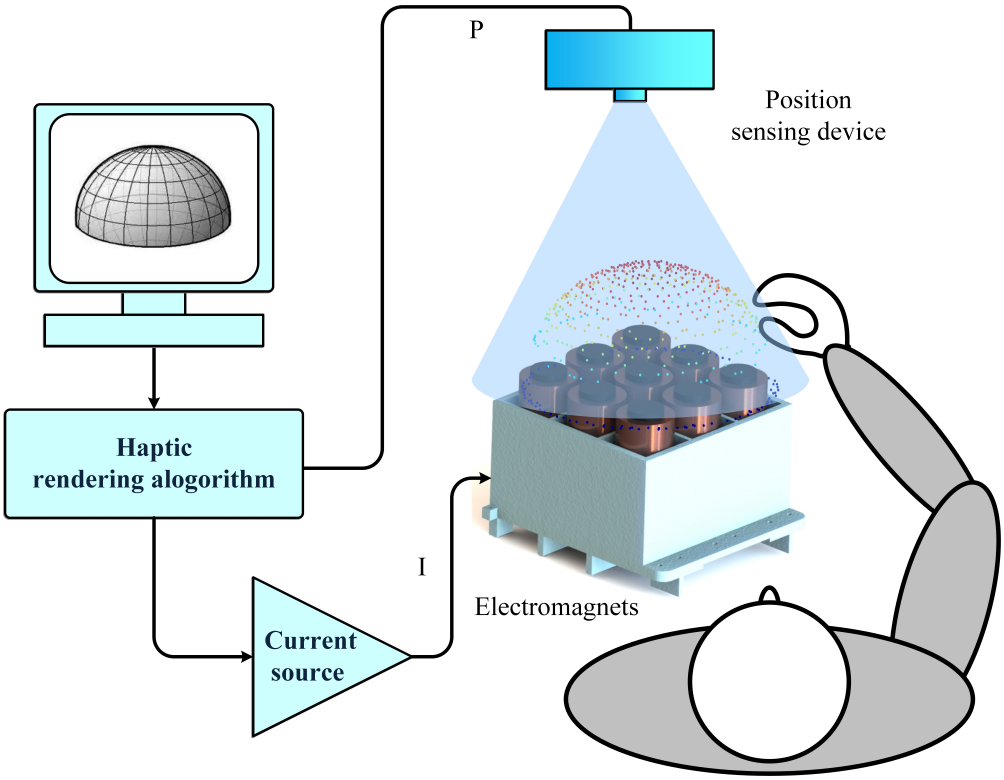

FIGURE 2.1: Haptic magnetic rendering of virtual objects in mid-air enables a participant to distinguish the features of three-dimensional (3D) virtual objects. The magnetic rendering is achieved using an electromagnetic-based haptic interface. This interface consists of an array of electromagnetic coils, a wearable orthopedic finger splint with a single magnetic dipole moment, and an impendence-type haptic rendering algorithm. Each coil is powered independently using a current source. A current input ($\mathbf{I} \in \mathbf{R}^{9\times1}$) is provided to the coils based on the geometry of the object and the position ($\mathbf{p} \in \mathbf{R}^{3\times1}$) of the user. The system exerts a controlled magnetic force based on the geometry of the 3D virtual objects and observations of participants are used to evaluate the system.

where $\nabla = \left[\frac{\partial}{\partial x}\frac{\partial}{\partial y}\frac{\partial}{\partial z}\right]^T$. Equation (2.1) can be rewritten as

$$\mathbf{F} = \begin{bmatrix} \frac{\partial \mathbf{B}(\mathbf{p})}{\partial x} & \frac{\partial \mathbf{B}(\mathbf{p})}{\partial y} & \frac{\partial \mathbf{B}(\mathbf{p})}{\partial z} \end{bmatrix}^\top \mathbf{m}, \tag{2.2}$$

where $\left[\frac{\partial \mathbf{B}}{\partial x}\frac{\partial \mathbf{B}}{\partial y}\frac{\partial \mathbf{B}}{\partial z}\right]$ is the magnetic field-derivative matrix. In a current free space, this matrix is symmetric and has zero trace due to equations 2.1 and 2.2 (Petruska and Nelson, 2015). The magnetic force components F_x, F_y, and F_z in (2.2) are calculated using

$$\begin{bmatrix} F_x \\ F_y \\ F_z \end{bmatrix} = \begin{bmatrix} \frac{\partial B_x(\mathbf{p})}{\partial x} & \frac{\partial B_y(\mathbf{p})}{\partial x} & \frac{\partial B_z(\mathbf{p})}{\partial x} \\ \frac{\partial B_x(\mathbf{p})}{\partial y} & \frac{\partial B_y(\mathbf{p})}{\partial y} & \frac{\partial B_z(\mathbf{p})}{\partial y} \\ \frac{\partial B_x(\mathbf{p})}{\partial z} & \frac{\partial B_y(\mathbf{p})}{\partial z} & \frac{\partial B_z(\mathbf{p})}{\partial z} \end{bmatrix} \begin{bmatrix} m_x \\ m_y \\ m_z \end{bmatrix}, \tag{2.3}$$

where m_x, m_y and m_z are the components of the magnetic dipole moment of the permanent magnet. Utilizing the constraints provided by the quasi-static simplifications on Maxwell equations, equation (2.3) can be rewritten as

$$\begin{bmatrix} F_x \\ F_y \\ F_z \end{bmatrix} = \begin{bmatrix} \frac{\partial \mathrm{B}_x(\mathbf{p})}{\partial x} & \frac{\partial \mathrm{B}_x(\mathbf{p})}{\partial y} & \frac{\partial \mathrm{B}_x(\mathbf{p})}{\partial z} \\ \frac{\partial \mathrm{B}_x(\mathbf{p})}{\partial y} & \frac{\partial \mathrm{B}_y(\mathbf{p})}{\partial y} & \frac{\partial \mathrm{B}_y(\mathbf{p})}{\partial z} \\ \frac{\partial \mathrm{B}_x(\mathbf{p})}{\partial z} & \frac{\partial \mathrm{B}_y(\mathbf{p})}{\partial z} & -\left(\frac{\partial \mathrm{B}_y(\mathbf{p})}{\partial y} + \frac{\partial \mathrm{B}_x(\mathbf{p})}{\partial x}\right) \end{bmatrix} \begin{bmatrix} m_x \\ m_y \\ m_z \end{bmatrix}. \tag{2.4}$$

Petruska and Nelson, 2015 showed that the roles of the dipole and the spatial derivatives of the field on the resulting force can be separated, equation (2.4) can be rearranged and the components of the dipole are factored out linearly. The magnetic force is given by

$$\begin{bmatrix} F_x \\ F_y \\ F_z \end{bmatrix} = \begin{bmatrix} m_x & m_y & m_z & 0 & 0 \\ 0 & m_x & 0 & m_y & m_z \\ -m_z & 0 & m_x & -m_z & m_y \end{bmatrix} \begin{bmatrix} \frac{\partial \mathrm{B}_x(\mathbf{p})}{\partial x} \\ \frac{\partial \mathrm{B}_x(\mathbf{p})}{\partial y} \\ \frac{\partial \mathrm{B}_x(\mathbf{p})}{\partial z} \\ \frac{\partial \mathrm{B}_y(\mathbf{p})}{\partial y} \\ \frac{\partial \mathrm{B}_y(\mathbf{p})}{\partial z} \end{bmatrix} = \boldsymbol{\mathcal{F}}(\mathbf{m})\mathbf{G}. \tag{2.5}$$

Next, let us consider the magnetic torque $\boldsymbol{\tau} \in \mathbb{R}^{3\times 1}$ acting on a dipole moment attached to the user finger splint when placed in a controlled magnetic field ($\mathbf{B}$). We can express the torque vector as the cross-product between the dipole and the field in units $\mathrm{N} \cdot \mathrm{m}$, with the torque attempting to align the dipole with the field:

$$\boldsymbol{\tau} = \mathbf{m} \times \mathbf{B}. \tag{2.6}$$

The cross product indicates that the torque generated is always perpendicular to both $\mathbf{m}$ and $\mathbf{B}$. This implies that it is impossible to generate torque about the $\mathbf{m}$ axis, regardless of the magnetic field. Therefore torque generation on a dipole is constrained to two degrees of freedom (DOFs), and thus force-torque generation to five DOFs. The cross product in (2.6) can be expressed in the skew-symmetric matrix form:

$$\mathbf{m} \times \mathbf{B} = \mathrm{Sk}(\mathbf{m})\mathbf{B}, \tag{2.7}$$

where

$$\mathrm{Sk}(\mathbf{m}) = \mathrm{Sk}\left(\begin{bmatrix} m_x \\ m_y \\ m_z \end{bmatrix}\right) = \begin{bmatrix} 0 & -m_z & m_y \\ m_z & 0 & -m_x \\ -m_y & m_x & 0 \end{bmatrix}. \tag{2.8}$$

The magnetic torque vector can be written such that the roles of the dipole and the field on the resulting torque are separated:

$$\boldsymbol{\tau} = \begin{bmatrix} 0 & -m_z & m_y \\ m_z & 0 & -m_x \\ -m_y & m_x & 0 \end{bmatrix} \begin{bmatrix} B_x(\mathbf{p}) \\ B_y(\mathbf{p}) \\ B_z(\mathbf{p}) \end{bmatrix}. \tag{2.9}$$

Using equations 2.5 and 2.9, one can express the force and torque generated using the EHI on a magnetic dipole in the position $\mathbf{p}$ as a function of the field and field derivative:

$$\begin{bmatrix} \boldsymbol{\tau} \\ \mathbf{F} \end{bmatrix} = \begin{bmatrix} \mathrm{Sk}(\mathbf{m}) & \mathbb{O} \\ \mathbb{O} & \boldsymbol{\mathcal{F}}(\mathbf{m}) \end{bmatrix} \begin{bmatrix} \mathbf{B} \\ \mathbf{G} \end{bmatrix}. \tag{2.10}$$

Since $\mathrm{Sk}(\mathbf{m})$ and $\boldsymbol{\mathcal{F}}(\mathbf{m})$ are constant for any permanent magnet attached to the user's fingertip, then by controlling the magnetic field and the magnetic field gradient generated by the EHI (equation 2.10), the required haptic forces and torques can be achieved.

2.1.1 Magnetic Field and Gradient Control

Magnetic force and torque are generated using an in-plane array of m electromagnetic coils, each electromagnet generates a magnetic field throughout its workspace that can be pre-calculated. The magnitude of this magnetic field and its gradient at any given position ($\mathbf{p} \in \mathbb{R}^{3\times 1}$) of the dipole moment varies linearly with the current through the electromagnet. The linear mapping between the generated magnetic field and the applied current can be represented by

$$\mathbf{B}(\mathbf{p}) = \tilde{\mathbf{B}}(\mathbf{p})\mathbf{I}, \tag{2.11}$$

where $\tilde{\mathbf{B}}(\mathbf{p})$ is the magnetic field current mapping at a point $\mathbf{p}$ and $\mathbf{I}$ is the applied current to a single electromagnet. The field current mapping can be found using the standard field modeling techniques, e.g., direct numerical integration, finite element modeling, or *in situ* field measurements. The total magnetic field at any given point within the workspace can be calculated using the superposition principle, it can be expressed as the linear combination

of the field contributions due to each of the electromagnetic coils

$$\mathbf{B}(\mathbf{p}) = \sum_{i=1}^{m} \mathbf{B}_i(\mathbf{p}) = \sum_{i=1}^{m} \tilde{\mathbf{B}}_i(\mathbf{p}) I_i \quad , \tag{2.12}$$

where $\mathbf{B}_i(\mathbf{p})$ is the magnetic field contribution due to the ith electromagnetic coil and I_i is the input current to the ith coil. With air-core electromagnets, the superposition principle is used and the field contributions of each of the coils to the total magnetic field are decoupled, and the flux densities can be individually pre-computed and then linearly superimposed. In the case of a soft-magnetic core electromagnet, if we assume a perfect soft-magnetic core with negligible hysteresis utilized, with all the cores of the coils operating in their linear magnetization region, the superposition principle is still valid. The total magnetic field generated using n in-plane electromagnetic coils as well as the derivative of the magnetic field in a given direction can be expressed as

$$\begin{bmatrix} \mathbf{B} \\ \mathbf{G} \end{bmatrix} = \begin{bmatrix} B_x(\mathbf{p}) \\ B_y(\mathbf{p}) \\ B_z(\mathbf{p}) \\ \frac{\partial \mathrm{B}_x(\mathbf{p})}{\partial x} \\ \frac{\partial \mathrm{B}_x(\mathbf{p})}{\partial y} \\ \frac{\partial \mathrm{B}_x(\mathbf{p})}{\partial z} \\ \frac{\partial \mathrm{B}_y(\mathbf{p})}{\partial y} \\ \frac{\partial \mathrm{B}_y(\mathbf{p})}{\partial z} \end{bmatrix} = \begin{bmatrix} \tilde{B}_{1x}(\mathbf{p}) & \tilde{B}_{2x}(\mathbf{p}) & \cdots & \tilde{B}_{mx}(\mathbf{p}) \\ \tilde{B}_{1y}(\mathbf{p}) & \tilde{B}_{2y}(\mathbf{p}) & \cdots & \tilde{B}_{my}(\mathbf{p}) \\ \tilde{B}_{1z}(\mathbf{p}) & \tilde{B}_{2z}(\mathbf{p}) & \cdots & \tilde{B}_{mz}(\mathbf{p}) \\ \frac{\partial \tilde{B}_{1x}(\mathbf{p})}{\partial x} & \frac{\partial \tilde{B}_{2x}(\mathbf{p})}{\partial x} & \cdots & \frac{\partial \tilde{B}_{mx}(\mathbf{p})}{\partial x} \\ \frac{\partial \tilde{B}_{1x}(\mathbf{p})}{\partial y} & \frac{\partial \tilde{B}_{2x}(\mathbf{p})}{\partial y} & \cdots & \frac{\partial \tilde{B}_{mx}(\mathbf{p})}{\partial y} \\ \frac{\partial \tilde{B}_{1x}(\mathbf{p})}{\partial z} & \frac{\partial \tilde{B}_{2x}(\mathbf{p})}{\partial z} & \cdots & \frac{\partial \tilde{B}_{mx}(\mathbf{p})}{\partial z} \\ \frac{\partial \tilde{B}_{1y}(\mathbf{p})}{\partial y} & \frac{\partial \tilde{B}_{2y}(\mathbf{p})}{\partial y} & \cdots & \frac{\partial \tilde{B}_{my}(\mathbf{p})}{\partial y} \\ \frac{\partial \tilde{B}_{1y}(\mathbf{p})}{\partial z} & \frac{\partial \tilde{B}_{2y}(\mathbf{p})}{\partial z} & \cdots & \frac{\partial \tilde{B}_{my}(\mathbf{p})}{\partial z} \end{bmatrix} \begin{bmatrix} I_1 \\ I_2 \\ \vdots \\ I_n \end{bmatrix} = \mathbb{F}_{8\times n}\mathbf{I} \quad , \tag{2.13}$$

where $\tilde{B}_{nx}(\mathbf{p})$, $\tilde{B}_{ny}(\mathbf{p})$ and $\tilde{B}_{nz}(\mathbf{p})$ are the magnetic field current mapping at point $\mathbf{p}$ of the field components from the n-th electromagnet along $x-$, $y-$and $z-$axis , respectively. and I_m is the input current applied on the m-th electromagnet.

The generation of the desired magnetic force and torque on a dipole attached to a finger splint at any given position within the rendering workspace can be viewed as a two-step process. First, the appropriate magnetic field and gradients (**B** and **G** matrices) corresponding to the desired force and torque are computed using equation 2.10. Second, The pre-calculated linear map between the magnetic field, field gradient, and the applied current is used to compute the required input currents to the coils of the electromagnetic haptic interface.

2.2 Electromagnetic Coils Design

The electromagnetic-based haptic device consists of an array of electromagnetic coils that generate controlled magnetic forces on a Neodymium permanent magnet (S-10-05-N, N52, nickel-plated, supermanete, Gottmadingen, Germany) with axial magnetization of $1.1579 \times 106\text{A.m}^{-1}$ and rated current of 2 A. The thickness and diameter of the permanent magnet are 10 mm and 10 mm, respectively. This magnet is attached to the tip of a wearable finger splint and enables the user to perceive the magnetic force. An electromagnet is built as a multi-layer electrical conductor -typically insulated copper wire- wound in the shape of a coil. Electromagnetic coils are designed with or without a core. In the case of designing coils with a ferromagnetic core which is utilized to amplify the field, an ideal soft magnetic material is used to avoid the effects of hysteresis. Air-core electromagnets are designed without any core, one advantage of using this type of coil is the simplicity of modeling and calculating the generated magnetic field another advantage is that multiple electromagnets are quasi-statically decoupled from each other. The design of ferromagnetic core electromagnets is an iterative process that relies heavily on Finite Element Analysis methods. When designing electromagnetic coils that are suitable for haptic rendering, the main three objectives are

- Achieve the maximum magnetic gradient and thus maximum magnetic force in a relatively large workspace, with a minimum of 0.8 mN which is the minimum force of the human sensory range.
- Control the strength, direction, and accuracy of the force produced by the electromagnetic interface at any given position in the workspace.
- Feasibility of the design, which includes manufacturing realities, size, and weight limitations that constrain the choice of parameters in the design.

Therefore, we optimize the design of the electromagnetic coils to satisfy this criterion while maintaining appropriate dimensions and response. The distance between the magnet and the coils is chosen to be fixed to 30 mm and the wire diameter is constant with a diameter of 0.7 mm. The inner- and outer diameter of the coil and its length are optimized using:

$$\begin{aligned} \underset{R_i, R_o, L_c}{\text{maximize}} \quad & F = m_z \frac{\partial B_z}{\partial z}\left(R_\text{i}, R_\text{o}, L_\text{c}\right) \\ \text{subject to} \quad & R_\text{c} < 6, \quad 5\tau < 100 \\ & R_\text{o} < R_\text{max} \quad , \quad L_\text{c} < L_\text{max}, \end{aligned} \tag{2.14}$$

where m_z is the dipole moment of the magnet and $\frac{\partial B_z}{\partial z}\left(R_\text{i}, R_\text{O}, L_\text{c}\right)$ is the gradient of the magnetic field with respect to the vertical direction. Further, R_i and R_o are the inner- and outer-diameter of the coil, respectively, and L_c is the length of the coil. This optimization problem provides optimal R_i, R_o, and L_c to maximize the generated force along z-axis.

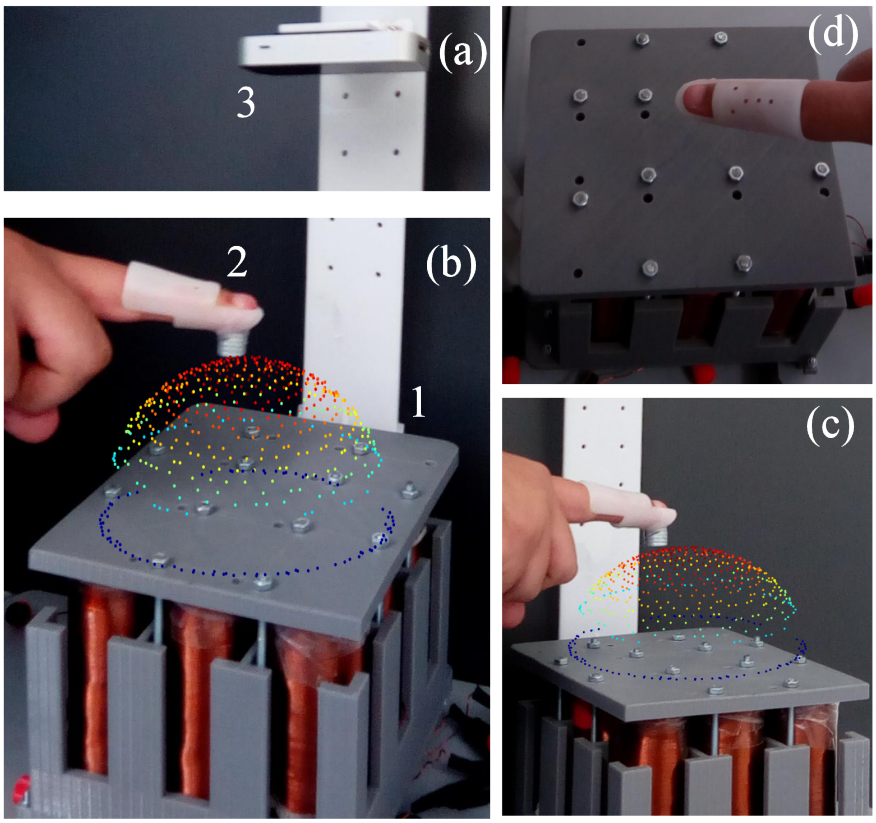

FIGURE 2.2: An electromagnetic-based haptic interface enables the operator to interact with virtual objects in three-dimensional (3D) space. (a) A position-sensing device is used to measure the position of the wearable finger splint in 3D space. (b) The position of the wearable finger splint is fed back to the control system to exert a magnetic force based on the rendered geometry. (c) Magnetic rendering of the half-sphere is achieved and participants distinguish its features with a success rate of 67.5%. (d) Participants distinguished this geometry in 65 seconds.

The first constraint limits the resistance of the coil below 6 Ω to enable the coil to draw approximately 6 A (coils are supplied with 36 V). The second constraint provides the time response of the coil $\tau = \frac{L_c}{R_c}$, where L_c and R_c are its inductance and resistance, respectively. The coil reaches its steady-state in approximately 100 ms. The third and fourth constraints define the maximum outer-diameter R_{max} and length L_{max} of each coil. This optimization is performed using MATLAB's *fmincon* function. This optimization routine is solved iteratively using the interior method for constrained non-linear optimization and we obtain a maximum force of 780 mN while satisfying the constraints given by (8). Each electromagnetic coil has inner and outer diameters of 24 mm and 38 mm, respectively. The height of the coil and the length of its low-carbon steel core are 100 mm and 110 mm, respectively. The number of turns is 1429.

2.3 Current Control Unit

Each of the electromagnets is independently supplied with current using electric drivers (MD10C, Cytron Technologies Sdn. Bhd, Kuala Lumpur, Malaysia). This driver can supply the coil with a current of up to 13A continuously. It offers sign-magnitude PWM signal

control mode with speed control PWM frequency up to 20KHz. In addition, it uses full solid-state components which result in faster response time and eliminates the wear and tear of the mechanical relay. Sign-magnitude PWM mode was used, and two control signals were used to control the speed and direction of the motor. PWM is used to control the speed while DIR is used to control the direction of the motor. All nine current values are sent to the controller using a PWM - I2C interface board (PCA9685, Adafruit Industries, New York, United States) with 16-channel 12-bit data resolution. The current is controlled via a MyRio control board (MyRio, National Instruments, Mopac, Expwy Austin, U.S.A).

The electromagnetic coils are fixed to upper and lower 3D-printed plastic frames (Ultimaker BV, Utrecht, Netherlands). It is designed to keep all magnetization axes parallel to each other. The electromagnetic configuration provides a planar footprint of 150 mm×150 mm and a height of 60 mm

Chapter 3

Localization system

3.1 Optical Localization System

The position and orientation of the operator's fingertip are tracked using the Leap Motion position sensing device (Leap Motion, San Francisco, CA, U.S.A). The controller consists of three IR (Infrared Light) emitters and two IR cameras. Hence, the Leap Motion controller can be categorized as a stereo-vision optical, marker-free tracking system. It creates a three-dimensional interaction space of 8 cubic feet above the device and a close range of around an inch above the controller. Through a combination of hardware and software, it senses hands, fingers, and tools.

The Leap Motion sensor is fixed above the electromagnetic configuration at a height of 50 cm. It can detect the hand from an altitude of 2.5 cm to 60 cm above the device. The Leap Motion controller library provides several features such as the velocity, length, and width of the finger in addition to the position and orientation of the finger in a pointing direction ($\mathbf{F_p}$). However, it does not provide information about the normal to the fingertip which represents the direction of the magnetic dipole ($\mathbf{m} \in \mathbf{R}^{3\times1}$) attached to the operator's finger. The normal vector to the palm ($\mathrm{P_n}$) as well as the instantaneous position vector ($\mathrm{F_p}$) in the pointing direction are continuously acquired from the sensor and used to calculate the position vector normal to the finger ($\mathrm{F_n}$) relative to the Leap Motion frame of reference

$$\mathrm{F_n} = (\mathrm{F_p} \times \mathrm{P_n}) \times \mathrm{F_p}. \tag{3.1}$$

The position vector normal to the finger relative to each of the nine electromagnetic coils ($\mathrm{F_{n_i}}$) is calculated as:

$$\vec{\mathrm{F}}_{\mathrm{n}_i} = \mathbf{H}_{\mathrm{LC}_i}\mathrm{F_n} \tag{3.2}$$

where $\mathbf{H}_{\mathrm{LC}_i}$ is a homogeneous transformation matrix from the Leap Motion reference frame to the ith electromagnetic coil frame

$$\mathbf{H}_{\mathrm{LC}_i} = \begin{bmatrix} \mathrm{R}_{\mathrm{LC}_i} & \mathrm{d}_{\mathrm{LC}_i} \\ 0 & 1 \end{bmatrix}$$

where $\mathbf{R}_{LC_i} \in \mathbf{R}^{3\times3}$ is a rotation matrix from Leap Motion reference frame to the ith

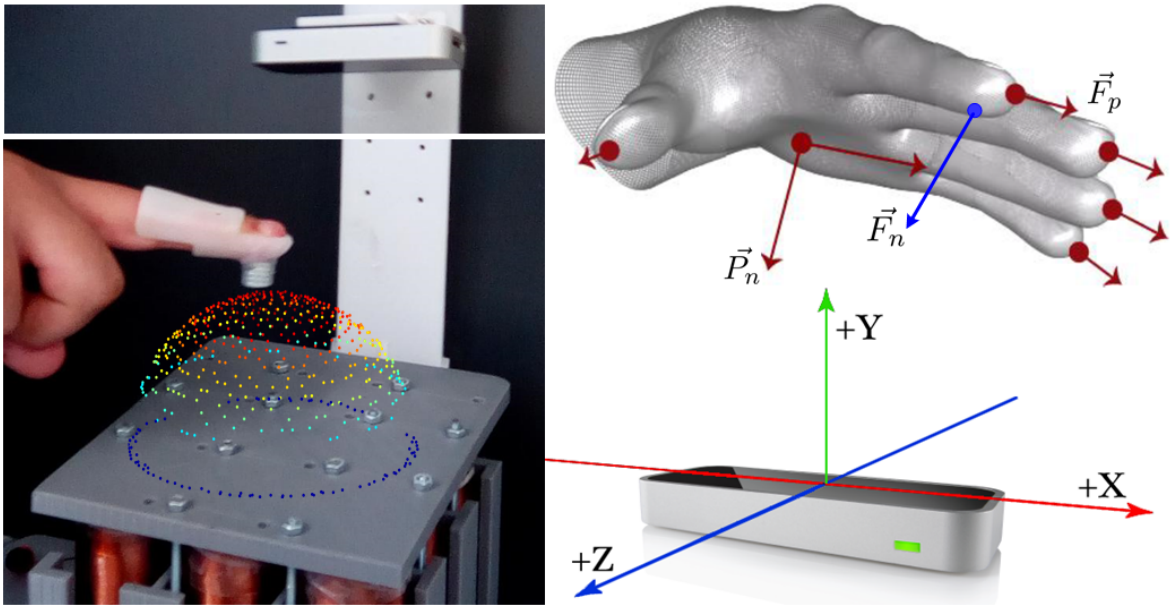

FIGURE 3.1: Localization system is developed for an EHI.

electromagnetic coil and $\mathbf{d}_{LC_i} \in \mathbf{R}^{3\times1}$ is the displacement vector from the center of the Leap Motion to the ith electromagnetic coil center.

3.2 Magnetic Localization System

Optical tracking techniques suffer from several limitations such as occlusions, high sensitivity to different illumination conditions, and computationally expensive sophisticated algorithms. Another limitation of optical tracking is that the line of sight between the tracked hand and the camera must always be clear. Keeping the tracked object within the sight of the camera limits the participant's range of movement. These limitations can be eliminated by using a magnetic-based localization system to estimate the position of the magnetic dipole attached to the user's finger.

A typical magnetic tracking system consists of one or more magnetic sources (transmitters), that induce electric voltage in one or more sensor modules (receivers). This voltage is a function in both the position and orientation of the magnetic source. Our magnetic localization system uses the magnetic symmetry of the EHI for the elimination of its field and does not depend on the pre-calculated magnetic field map of the source. The system utilizes two identical arrays of three-dimensional (3D) magnetic field sensors. These arrays are mounted above and below the EHI. The upper layer of magnetic field sensors is used to sense the magnetic field from the permanent magnet and the electromagnetic coils. The lower layer of magnetic field sensors is used to sense the magnetic field from the electromagnetic coils. The subtraction of the magnetic field between these two arrays provides the field of the magnetic dipole. Figure 3.2 shows a schematic representation of the system.

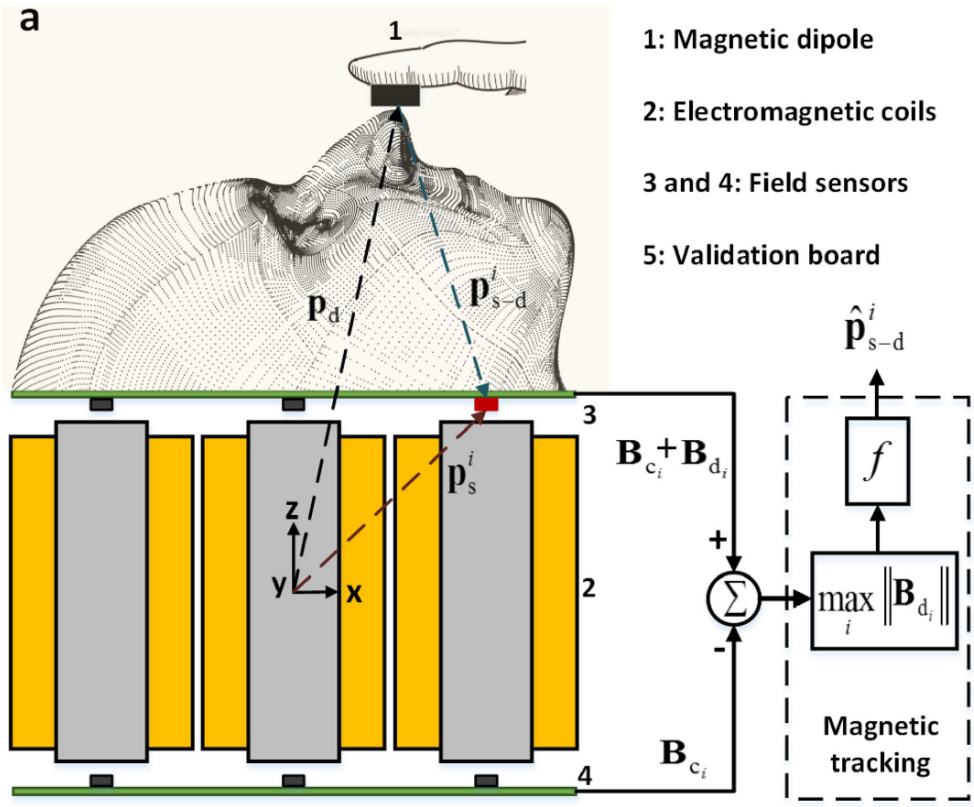

FIGURE 3.2: Localization system is developed for an EHI. Schematic representation shows a magnetic dipole (1) and a planar configuration of electromagnetic coils (2). The magnetic localization system consists of two identical arrays of 3D magnetic field sensors. The first (3) and second (4) arrays are fixed above and below the EHI, respectively.

3.2.1 Magnetic Localization System Description

The system consists of two identical arrays of magnetic field sensors, each array contains nine 3D Hall effect sensors (3D magnetic sensor TLV493DA1B6, Infineon Technologies AG, Munich, Germany). The sensitivity of the sensors is 0.1 mT within a range of ±130 mT, and they are validated using a calibrated three-axis digital teslameter (Senis AG, 3MH3A-0.1200mT, Neuhofstrasse, Switzerland). The Hall effect sensor can detect the magnetic dipole in a workspace of 50mm x 50mm x 50 mm. The two arrays are located at the same height of 14 mm from the EHI. This sensor is located at the center of the corresponding coil.

3.2.2 Localization Algorithm

Magnetic force is applied on a dipole attached to a wearable finger splint ($\mathbf{m} \in \mathbf{R}^{3\times1}$) using a controlled magnetic field $\mathbf{B}(\mathbf{p}) \in \mathbf{R}^{3\times1}$ at point ($\mathbf{p}$) generated from an in-plane array of n electromagnetic coils. Two arrays of m magnetic field sensors are mounted above and below the electromagnetic coils and used to estimate the position of the magnetic dipole $\mathbf{p}_d$. The total magnetic field at the ith sensor mounted on the upper array ($\mathbf{B}^i_{su}$) is

$$\mathbf{B}^i_{su} = \mathbf{B}_{di} + \sum_{j=1}^{n} \mathbf{B}_{c_{ij}}$$

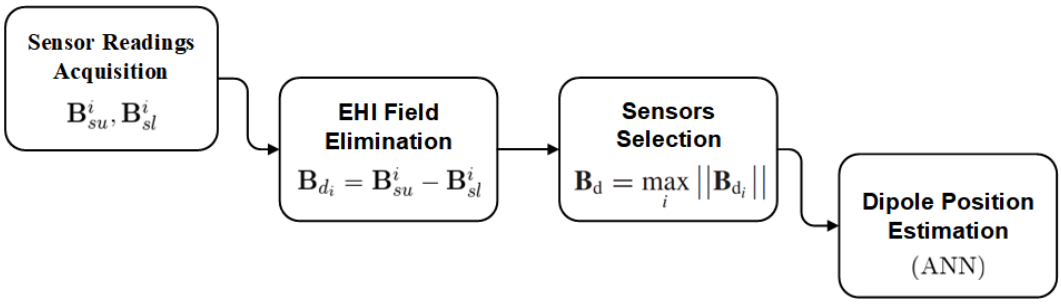

FIGURE 3.3: Magnetic localization algorithm. The magnetic field measurements are acquired from both the upper and the lower sensors array, the magnetic field due to the EHI is eliminated by subtracting the magnetic field measurements of the upper array from that of the lower array. The magnetic field sensor measures the maximum value after subtraction in selected and fed to an artificial neural network (ANN) to estimate the position of the finger magnet.

where $\mathbf{B}_{di}$ and $\mathbf{B}_{\mathrm{c}_{ij}}$ are the magnetic field generated by the dipole and the contribution of the magnetic field generated by the jth coil, respectively. The superimposed field $\mathbf{B}_{\mathrm{c}_{ij}}$ can be measured directly from the corresponding ith sensor at the lower array due to the magnetic symmetry of the EHI without modeling. Therefore, the magnetic field affecting the ith sensor on the lower array $\mathbf{B}^i_{sl}$ is given by

$$B^i_{sl} = \sum_{j=1}^{n} \mathbf{B}_{\mathrm{c}_{ij}}$$

The magnetic field generated by the dipole ($\mathbf{B}_{di}$) attached to the wearable finger splint can be now measured directly by subtracting the total magnetic field at the sensor mounted on the upper array from the magnetic field at the sensor mounted on the lower array (EHI field)

$$\mathbf{B}_{di} = \mathbf{B}^i_{su} - \mathbf{B}^i_{sl}$$

In order to estimate the position of the magnetic dipole $\mathbf{p}_d$, the magnetic field measurement of the nearest ith sensor to the magnetic dipole $\mathbf{B}_\mathrm{d}$ is selected, which is given by

$$\mathbf{B}_\mathrm{d} = \max_i ||\mathbf{B}_{\mathrm{d}_i}||$$

Then, the estimated position of the magnetic dipole with respect to the ith sensor $\left(\mathbf{p}^i_{s-d}\right)$ is determined by a function (f) that maps the input dipole magnetic field ($\mathbf{B}_\mathrm{d}$) to its position. A feed-forward artificial neural network (ANN) is trained to approximate this function and used to estimate the magnetic dipole position in real time without iterations [Cybenko, 1989]. MATLAB neural net fitting toolbox is utilized for building and training this network using 1300 data points in a workspace of 50 mm x 50 mm x 50 mm around the magnetic dipole. The trained neural network consists of an input layer, an output layer, and ten hidden layers; each contains ten neurons. The neural network is trained using a back-propagation learning algorithm and is implemented using the Levenberg–Marquardt technique. Figure 3.4 shows the residual mean position error of the neural network after training, the coefficient of determination is 0.999 and the mean absolute position error

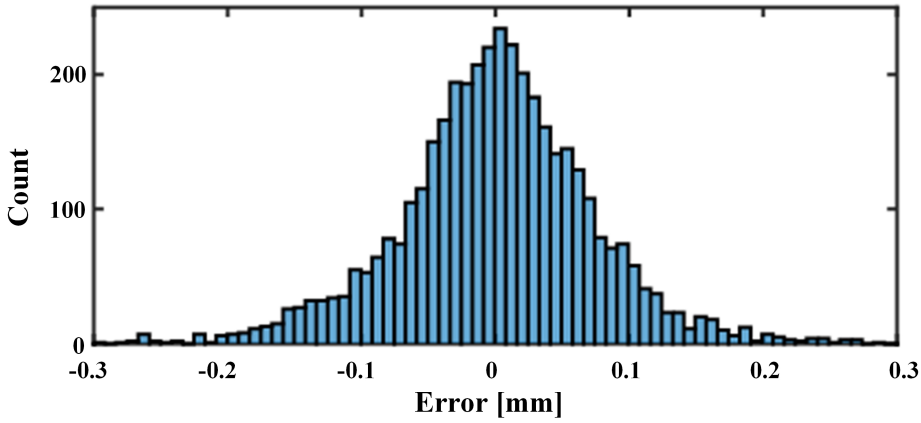

FIGURE 3.4: Histogram of the residual mean position error for the trained neural network is calculated with a coefficient of determination of 0.999.

(**MAE**) is 0.055 mm. Each data point used to train the ANN contains the 3D field data ($\mathbf{B}_{\mathrm{m}}$) for a given position ($\mathbf{p}$) along $x-, y-$ and $z-$axis. These field points are calculated by

$$\mathbf{B}_m = -\mu_0 \nabla \phi(\mathbf{p})$$

where μ_0 is the magnetic permeability of free space and $\phi(\mathbf{p})$ is the magnetic scalar potential. Finally, the position of the magnetic dipole with respect to the EHI frame of reference $\mathbf{B}_{\mathrm{d}}$ is calculated using (see figure 3.2.)

$$\mathbf{p}_d = \mathbf{p}_s^i - \mathbf{p}_{s-d}^i$$

where $\mathbf{p}_s^i$ is a fixed position vector from the center of the EHI frame to the ith sensor. The position of the magnetic dipole is used to validate the localization system under different cases of the field generated by the EHI.

3.2.3 Magnetic Tracking Validation

Validation experiments are conducted under four different cases of the magnetic field generated by the EHI. These cases will likely be encountered during the haptic rendering of virtual shapes. In these experiments, the estimated position is generated by Cases 1-4 and compared to the actual position. In all cases, the localization system is tested using two conditions. First, the magnetic dipole is fixed in circular holes ($n = 25$), which are distributed on a validation board. At every hole, we repeat the trails ($n = 5$) to calculate the MAE between the estimated and actual position of the hole and to investigate the repeatability of the localization system. Second, the magnetic dipole is moved along a slot located on a validation board. This slot guides the magnetic dipole to move in a predefined path. We repeat this trail (n = 6) for the four different cases of the field generated by the EHI. The magnetic localization system is validated in the absence of the field generated by the EHI

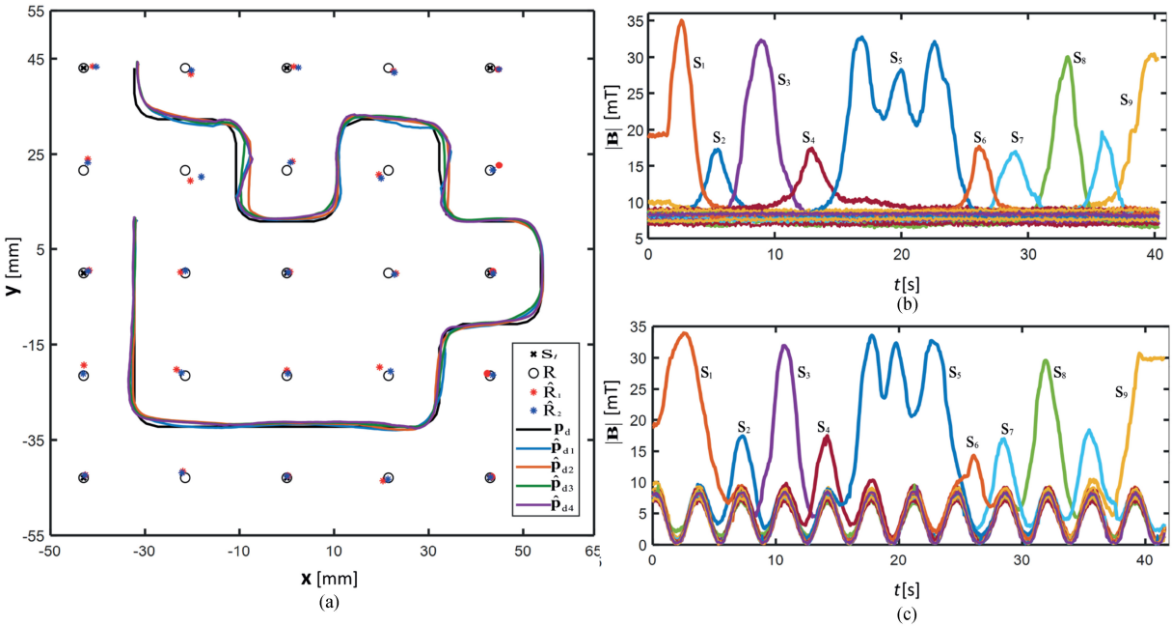

FIGURE 3.5: Magnetic localization system is experimentally validated. (a) Results of the estimated position using S_i sensors under the absence $\hat{R}_1$ and the presence $\hat{R}_2$ of the magnetic field generated by the EHI for 25 different reference points R and a predefined path $\mathbf{p_d}$ in a two-dimensional validation board. This test is performed under four different cases of the field generated by the EHI. Zero (Case 1), static (Case 2), sinusoidal (Case 3), and time-varying magnetic field (Case 4). $\hat{\mathbf{p}}_{d1}, \hat{\mathbf{p}}_{d2}, \hat{\mathbf{p}}_{d3}$, and $\hat{\mathbf{p}}_{d4}$ are the estimated paths for Cases 1-4, respectively. (b) Resultant magnetic field generated by the magnetic dipole and the EHI during Case 2 for the ith sensor. (c) Resultant magnetic fields generated by the magnetic dipole and the EHI are measured in Case 3 for the ith sensor.

(Case 1), and the estimated positions of the magnetic dipole in the first and second conditions are shown in Fig. 3.5(a). In the second and third cases, the electromagnetic coils are supplied with static (Case 2) and sinusoidal (Case 3) current inputs of 0.65 A, respectively. The electric noise in the current affects the generated magnetic fields. However, the fields of adjacent coils within the vicinity of the magnetic dipole are used to estimate its position. Therefore, the influence of the electric noise is minimized by the field subtraction. The estimated positions of the magnetic dipole in the second testing condition are shown in Fig. 3.5(a). The measurements of the resultant magnetic field for the ith sensor are shown in Fig. 3.5(b) and (c), respectively. In Case 4, the localization system is tested under time-varying magnetic fields. The coils are supplied by time-varying inputs current with a peak value of 1 A, the estimated positions of the magnetic dipole in the second testing condition are shown in Fig. 3.5(a). The MAE is calculated for the four cases ($n = 125$), 0.80 ± 0.30 mm, 1.26 ± 0.43 mm, 0.91 ± 0.33 mm, and 0.86 ± 0.33 mm for Cases 1-4, respectively. The estimated position data are examined using the Gage study (crossed), test-retest component to investigate the repeatability of the localization system. This test shows the percentage of variation caused by the measurement system of the total variation in the process under the same conditions. Using the analysis of variance method, this test suggests that the percentages of variation are $3.50 \pm 1.15\%$, $4.90 \pm 1.65\%$, $3.75 \pm 1.30\%$, and $3.50 \pm 1.15\%$ for Cases 1–4, respectively. Our analysis shows statistical evidence to conclude that the repeatability of the proposed

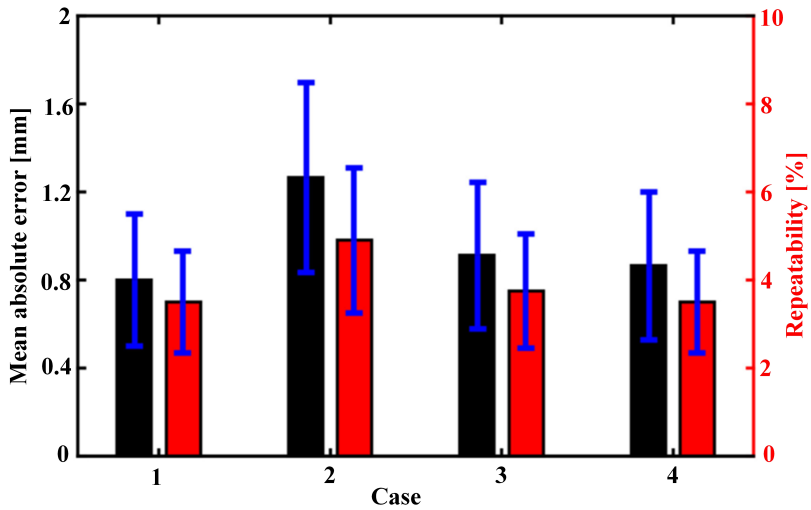

FIGURE 3.6: Accuracy and the repeatability of the magnetic localization system are experimentally investigated for Cases 1-4, respectively. Our statistical analysis shows that the repeatability of the localization system is acceptable, at $\alpha = 0.05$ and 95% confidence level.

localization system is acceptable regardless of the field generated by the EHI, at 95% confidence level. The total MAEs in the absence and presence of the magnetic field generated by the EHI are $0.80 \pm 0.30 (n = 125)$ and 1.01 ± 0.45 mm ($n = 375$), respectively. The difference between these errors is 0.21 mm which is less than the standard deviation of the MAEs. We attribute this variation to the mechanical error in the assembly of the two arrays of magnetic field sensors and the electric noise of the coil current inputs. The localization accuracy can be improved by decreasing the mechanical assembly error and using magnetic field sensors with relatively higher sensitivity.

Chapter 4

Haptic Rendering

Haptic rendering is defined as the method of computing and generating forces in response to user interactions with virtual objects based on measurements of the operator motion. Itbn enables a user to touch, feel, and manipulate virtual objects through a hapticinterface. Haptic rendering requires a haptic interface which maps the force signal from the computer into a force that the operator can perceive, a virtual environment, and a haptic rendering algorithm according to which the two are linked. Different haptic rendering algorithms have been proposed over the past 25 years. These algorithms can be classified according to

- Probing object modeling
- Number of degrees of freedom (DoFs)
- Control type
- Feedback type
- Interaction type

4.1 Magnetic Haptic Rendering Algorithm

Magnetic rendering is the process of generating mid-air haptic feedback sensation via magnetic forces exerted on a dipole attached to an interaction tool. This magnetic force is achieved using an electromagnetic-based haptic interface (EHI). This interface consists of an array of electromagnetic coils that are powered independently to exert controlled magnetic force, a wearable orthopedic finger splint with a single magnetic dipole moment, and a dipole position localization system all with an impedance-type haptic rendering algorithm. Magnetic rendering of a 3D virtual object is achieved using magnetic forces exerted on wearable device. This haptic feedback enables a participant to distinguish the volumetric features of a three-dimensional (3D) virtual objects in mid-air.

First, the constraint surface of the virtual object is extracted from its computer-aided design (CAD) model, and discretized into point cloud. Each point is mapped into constraint force based on the geometry of the rendered shape. For each shape a force constant is calculated which maps the geometry of the rendered object to the force capabilities of the magnetic haptic interface. These constraint forces lay perpendicular to the surface and are

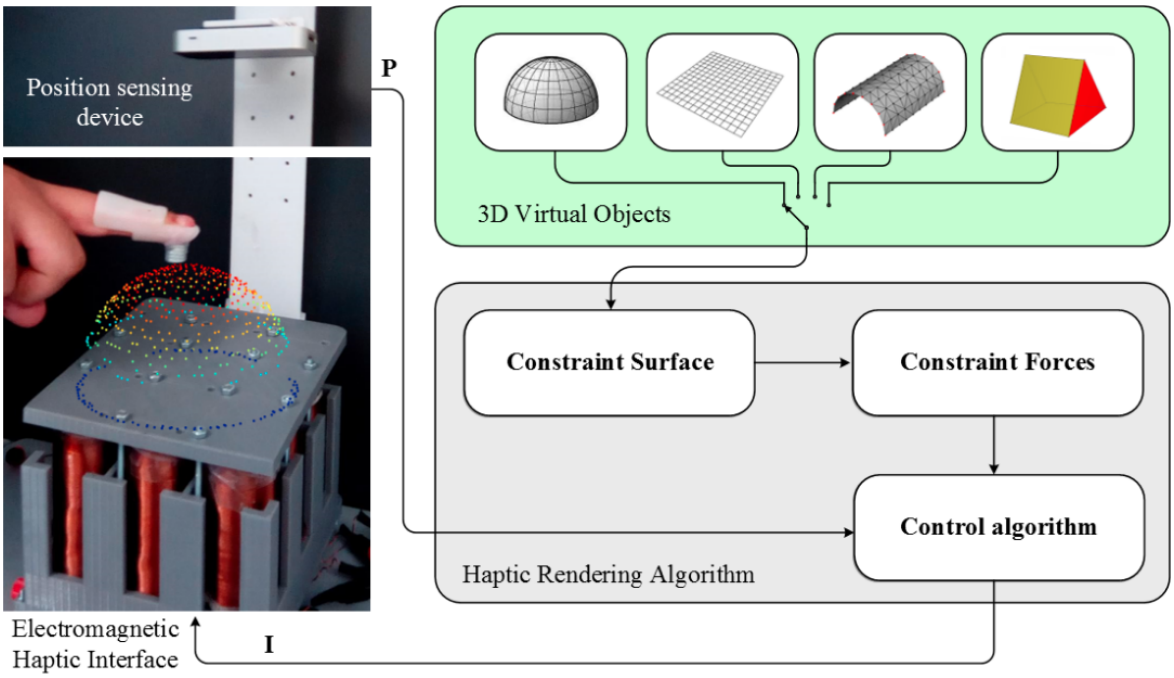

FIGURE 4.1: An electromagnetic-based haptic interface enables the operator to interact with virtual objects in mid-air. A position sensing device is used to measure the position of the wearable finger splint in 3D space. Position of the wearable finger splint is fed back to an impedance-type haptic rendering algorithm to exert a magnetic force based on the rendered three-dimensional (3D) virtual object geometry(flat, half-sphere, half-cylinder, and wedge).

provided as reference inputs to a control system that calculates the current inputs to the electromagnetic coils. The objective of the control system is to generate a set of current inputs that minimizes the error between the constraint force of the virtual object and the exerted magnetic force on the dipole of the orthopedic finger splint based on the pose of the finger. An optical position sensing device (Leap Motion, San Francisco, CA, USA) along with a magnetic localization system measures the six-degree-of freedom pose of the finger during interaction with the virtual objects. It is also possible to render virtual objects without measuring the pose of the finger. In this case, the current inputs to the coils are optimized such that the error between the constraint force of an object and the rendered magnetic forces is minimized. Each coil is powered independently using a current source. A current input ($I \in R^{9\times1}$) is provided to the coils based on the geometry of the object and the position ($p \in R^{3\times1}$)of the user. The system exerts a controlled magnetic force based on the geometry of the 3D virtual objects and observations of participants are used to evaluate the system.

4.1.1 Constraint Surface Forces

The virtual object provides the constraint surface g(r, t) = 0. Therefore, the constraint surface results in a constraint force $\mathbf{F_s}$ that lay perpendicular to the surface and is given by

$$\mathbf{F_s} = \lambda \nabla g(\mathbf{r}, t), \tag{4.1}$$

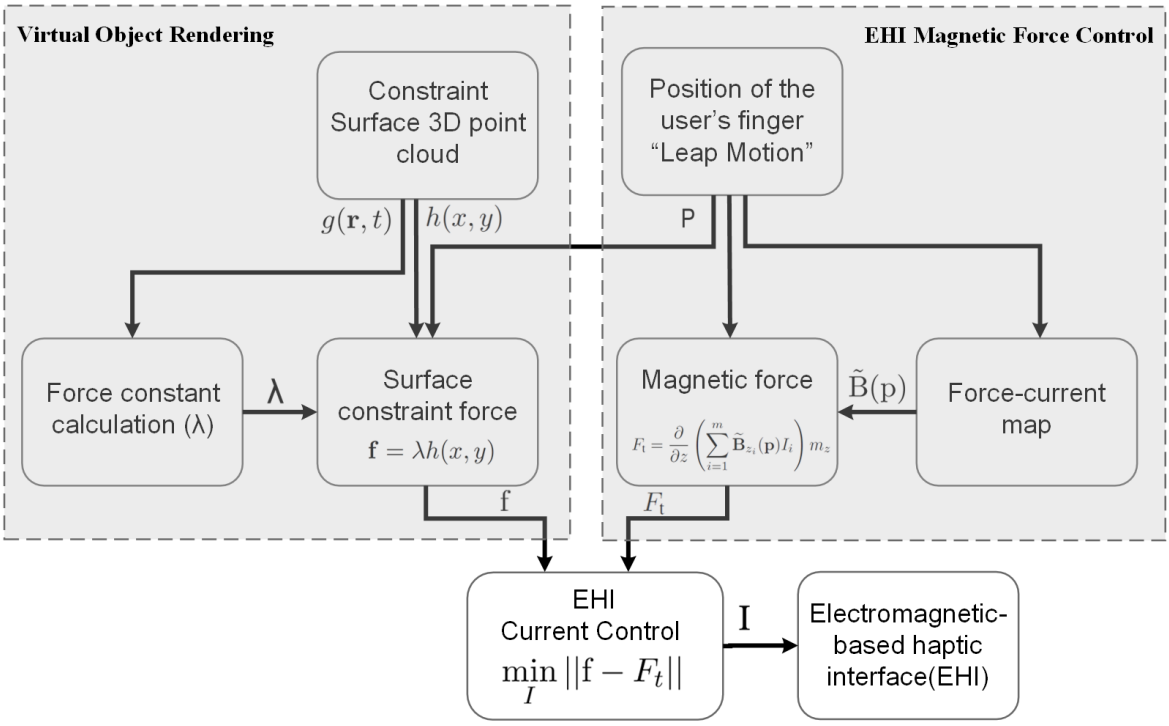

FIGURE 4.2: Magnetic Rendering Algorithm.

where $\mathbf{r} \in \mathbf{R}^{3\times 1}$ is the position of a point on the constraint surface $g(\mathbf{r}, t)$ and λ is a force constant. The force constant maps the geometry of the rendered object to the force capabilities of the magnetic haptic interface. This constant λ controls the values of the constraint forces. In the case of selecting relatively large values forλ, for which f is relatively large, an increase in the force error can result in relatively large current inputs that are not viable due to the constraints on the currents input to the EHI. On the other hand, the ability of the operator to perceive the virtual shape is decreased for relatively small values of the force constant . Therefore, we define an error function that represents the mean squared error between the constraint forces and the generated magnetic force

$$e(\lambda, \mathbf{I}) = \frac{1}{n}\sum_{j=1}^{n}\left\|\lambda h\left(x_j, y_j\right) - \sum_{i=1}^{m} I_i \frac{\partial \widetilde{B}_{z_i}(\mathbf{p})}{\partial z} m_z\right\|^2, \tag{4.2}$$

where n is the number of points on the constraint surface of the virtual object. Equation (4.2) is used in the following optimization problem

$$\begin{aligned} \max_{\lambda} \quad \min_{\mathbf{I}} \quad & e(\lambda, \mathbf{I}) \\ \text{subject to} \quad & 0 < I_i \leq u_i, \quad i = 1, \ldots, m \\ & \textstyle\sum_{i=1}^{m} I_i \leq I_t, \quad i = 1, \ldots, m. \end{aligned} \tag{4.3}$$

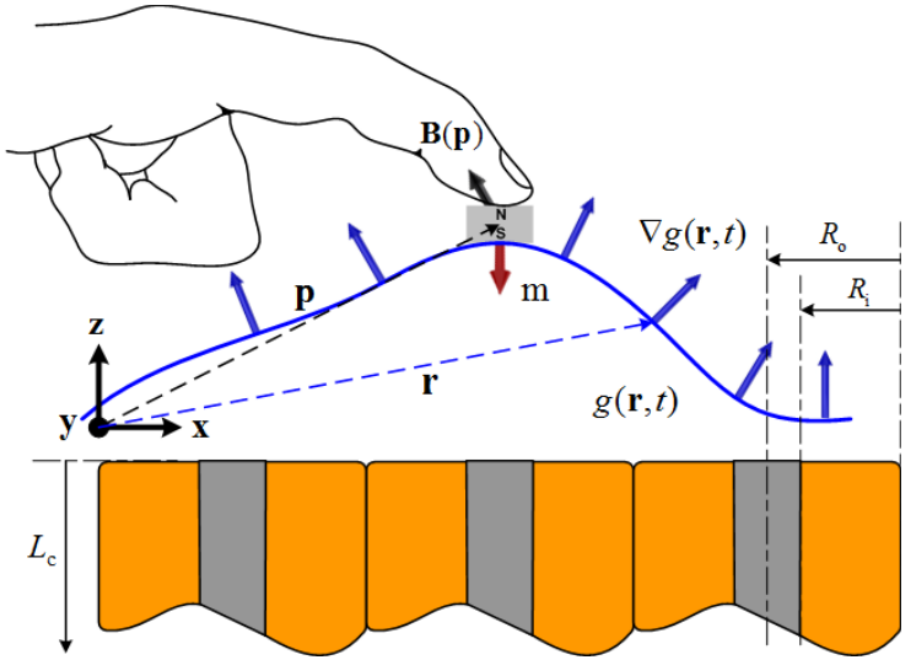

FIGURE 4.3: The constraint surface $g(r,t)$ of the virtual object (blue curve) provides a constraint force $g(r,t)$. Magnetic field $B(p)$ at a point p exerts a magnetic force on the magnetic dipole **m**. This magnetic dipole is attached to the operator via an orthopedic finger splint, and its position is measured using a position localization system. The variables R_i, R_o, and L_c represent the inner-diameter, outer-diameter, and length of the coil, respectively. Note that **r** is the position of a point on the constraint surface

This optimization is solved only once offline for each 3D virtual object to obtain the force constant prior to the rendering process.

The steps required to render a virtual heart are shown in figure 4.4. A 3D model of the heart is developed and deployed on the electromagnetic system. The Digital Imaging and Communications in Medicine (DICOM) file is converted to nearly raw raster data (NRRD) format and then stored as an STL file (Figure 4.4(a)). The model constraint surface is simultaneously converted and stored in the form of point cloud data and is saved as a PLY file (Figure 4.4 (b)). Preprocessing techniques are applied to the data to clean it up and downsample the large-scale data. Each point is mapped onto a constraint force based on the height of the entire model and within the sensory range of humans (minimum of 0.8mN), as shown in Figure 4.4(c). The difference between the constraint force of the heart and the generated magnetic forces is minimized while the participant slides one finger along the virtual trajectories. The observed magnetic forces are calculated during interaction with the virtual heart, as shown in Figure 4.4(d). Our system enables the rendering of one side (upper side) of the heart only due to the planar configuration of the electromagnetic coils. Therefore, it is not possible to interact with the lower side of the virtual object with the system in its current configuration. Nevertheless, it is possible to rotate the 3D object and recalculate the magnetic forces to allow the participant to fully interact with its boundaries

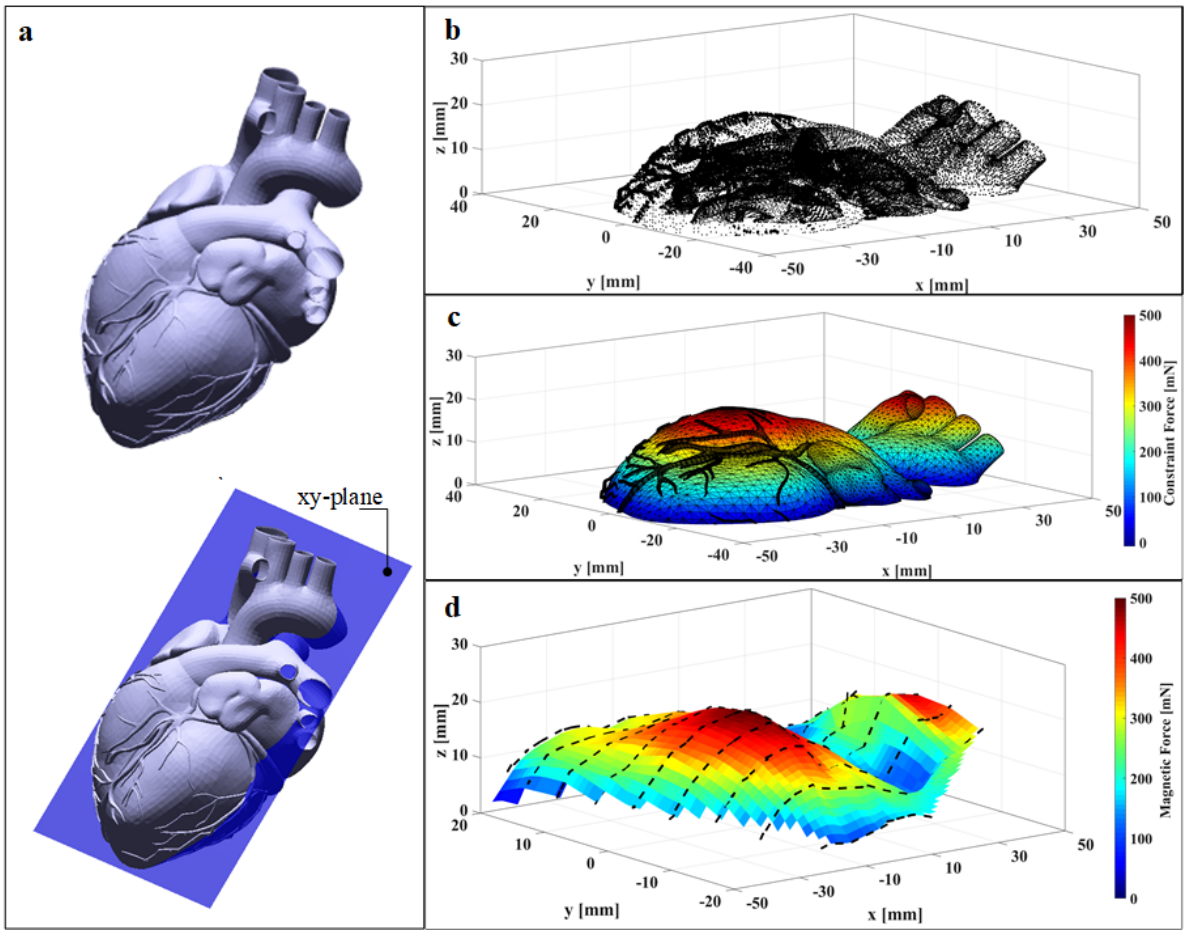

FIGURE 4.4: Three-dimensional model of a heart is modeled and programmed into a head-mounted display. The boundaries of the heart are magnetically rendered to enable participants to interact with its surface. (a) A model of the heart is generated and its upper half is extracted. (b) A point cloud is generated for the heart. (c) Each point is mapped into a constraint force that is greater than the sensory range of humans. (d) The trajectories taken during interaction with the virtual heart indicate that the operator slides one finger on its boundaries using visual and force feedback

4.1.2 Magnetic Forces

Magnetic fields are generated using an in-plane array of electromagnetic coils. We apply controlled magnetic force on the finger splint (Fig. 4.3) with a single magnetic dipole moment ($\mathrm{m} \in R^{3\times1}$) using controlled magnetic field ($\mathrm{B(p)} \in R^{3\times1}$). Let ($\mathrm{p} \in R^{3\times1}$)be the position of the permanent magnet attached to the finger splint. If a controlled magnetic field is applied using a configuration of planar electromagnetic coils then a magnetic force ($\mathrm{F_m} \in R^{3\times1}$) is generated and is given by

$$\mathbf{F_m} = \sum_{i=1}^{n} \nabla(\mathbf{m} \cdot \tilde{\mathbf{B}}_i(\mathbf{p}))I_i, \tag{4.4}$$

where $\tilde{\mathbf{B}}_i(\mathbf{p})$ is the magnetic field current mapping and I_i is the input current to the ith electromagnetic coil. The magnetic force component ($\mathrm{F_z}$) along the z-axis is responsible for

rendering the geometry of the virtual object and is given by

$$F_z = \frac{\partial \widetilde{\mathbf{B}}_x(\mathbf{p})\mathbf{I}}{\partial z} m_x + \frac{\partial \widetilde{\mathbf{B}}_y(\mathbf{p})\mathbf{I}}{\partial z} m_y + \frac{\partial \tilde{\mathbf{B}}_z(\mathbf{p})\mathbf{I}}{\partial z} m_z. \tag{4.5}$$

where $\widetilde{\mathbf{B}}_x(\mathbf{p})$, $\widetilde{\mathbf{B}}_y(\mathbf{p})$, $\widetilde{\mathbf{B}}_z(\mathbf{p})$ are the magnetic field current mapping at a point p of the field components along x-, y- and z-axis, respectively. And m_x, m_y, m_z are the components of the magnetic dipole moment of the permanent magnet. The components of the magnetic dipole moment along x- and y-axis (m_x and m_y) are relatively smaller than m_z. Therefore, Consequently, to simplify the analysis in this investigation, the orientation of the dipole is constrained to move in the z-axis. The superposition principle [Khalil, Abelmann, and Misra, 2014] is used and Equation 4.5 is simplified as follows:

$$F_{\mathrm{t}} = \frac{\partial}{\partial z} \left(\sum_{i=1}^{m} \widetilde{\mathbf{B}}_{z_i}(\mathbf{p}) I_i \right) m_z \tag{4.6}$$

where F_{t} is the total magnetic force exerted on the magnetic dipole. Further, I_i and $\widetilde{\mathbf{B}}_{z_i}$ are the ith current input and the ith field-current map, respectively.

4.1.3 Current Control Algorithm

The control system generates an optimal set of current inputs to the EHI that minimizes the error between the required surface constraint force of the virtual object and the controlled magnetic force. Therefore, we define the following error function $(\epsilon(\mathbf{I}))$

$$\epsilon(\mathbf{I}) = \|\mathbf{F_s} - \mathbf{F_m}\|, \tag{4.7}$$

solving for both the surface constraint force and the magnetic force. Equation 4.7 can be written as

$$\epsilon(\mathbf{I}) = \|\lambda \nabla g(\mathbf{r}, t) - \frac{\partial}{\partial z} \left(\sum_{i=1}^{m} \tilde{\mathbf{B}}_{z_i}(\mathbf{p}) I_i \right) m_z\| \tag{4.8}$$

The objective is to find the optimal current that minimizes the error between the required magnetic force and the controlled magnetic force. Therefore, we use the error function $(\epsilon(\mathbf{I}))$ to formulate the following optimization objective function:

$$\begin{aligned} \underset{\mathrm{I}}{\text{minimize}} \quad & e(\mathrm{I}) = \|\epsilon(\mathrm{I})\| \\ \text{subject to} \quad & 0 < I_i \leq u_i, \quad i = 1, \ldots, m \\ & \textstyle\sum_{i=1}^{m} I_i \leq I_{\mathrm{t}}, \quad i = 1, \ldots, m \end{aligned} \tag{4.9}$$

where $e(\mathrm{I})$ is a scalar objective function to be minimized using I. Further, I_i is the input current to the ith electromagnetic coil, u_i is an upper limit on the input current, and I_t is the maximum current provided via a power source. The optimization is performed using

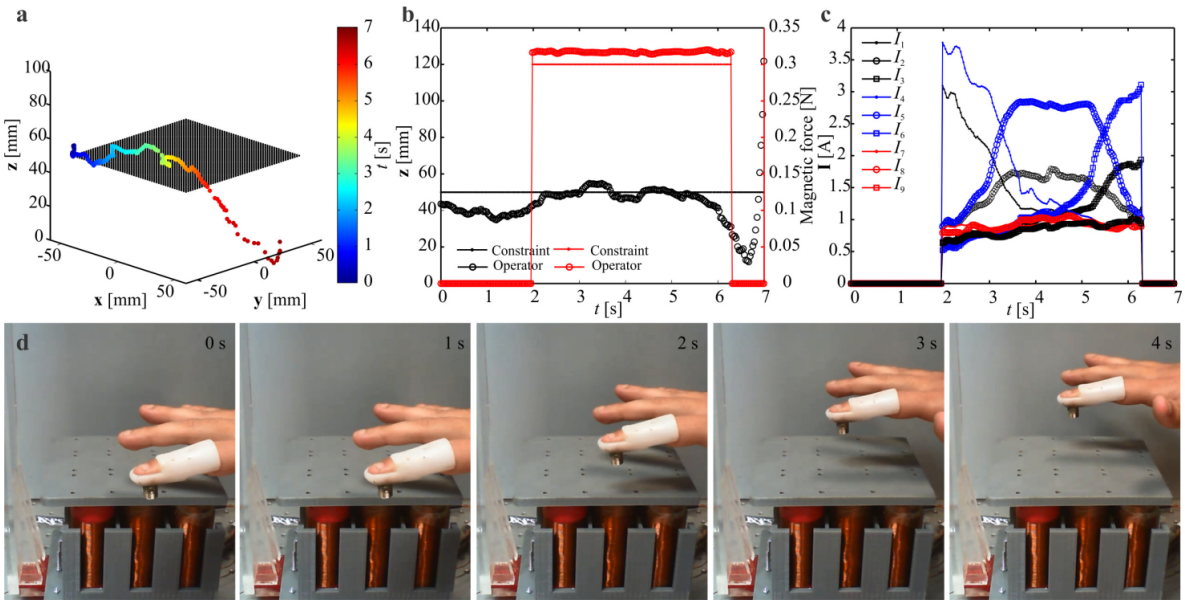

FIGURE 4.5: A representative magnetic rendering of a flat surface (at a height of 50 mm) shows the position of the operator and the calculated forces and currents during shape differentiation. (a) The constraint $(g(r,t))$ of the flat surface is decomposed into 3721 points (small black circles). The trajectory of the finger splint indicates a deviation from the rendered flat surface only outside the workspace of the system. (b) The position of the finger splint along the z-axis indicates a maximum deviation of 14 mm from the flat surface during this trial. At the time, $t = 6$ second, the participant moves outside the workspace of the system. (c) Current inputs are calculated and supplied to the electromagnetic coils based on the position of the wearable finger split during this trial. (d) The participant slides his finger on the surface several times. The successful participants differentiate the virtual flat surface from other objects in 92 seconds.

the Levenberg-Marquardt algorithm from MATLAB 8.4 (R2014b, The MathWorks, Inc., Massachusetts, USA). Therefore, the optimization adapts the input currents simultaneously to exert a magnetic force on the user's finger during the rendering process.

4.2 Magnetic Rendering Validation

Haptic rendering of a virtual 3D object is achieved by generating its constraint surface. The surface constraint is discretized into 3D points. This step is followed by the calculation of the force constant λ by solving (4.3) using MATLAB $fminmax$ function. This optimization routine is performed only once for each object. The current input to the electromagnetic coils is calculated by solving (4.9) using MATLAB $fmincon$ function.

4.2.1 Magnetic Rendering of a Virtual Flat Surface

Magnetic rendering of a virtual flat surface the constrained surface point cloud obtained from the shape CAD or a 3D scanner is used to compute the force constant and the surface constraint forces. Knowing the user finger position and the force current map the repulsive magnetic force can be calculated. The optimal current signals are computed and fed to the electromagnetic based haptic interface. Fig. 4.5(a) shows 3721 points that span a flat surface. These points are generated using the CAD model of a flat surface after preprocessing to

down sample the large scale data. The flat surface has an edge length of 100 mm and is located at hight of 50 mm along z-axis of the EHI. A force constant (λ) for this flat surface placed at this particular height above the EHI is then calculated by solving the optimization problem (4.3) using MATLAB $fminmax$. The force constant (λ) calculated for rendering the virtual surface is 6 N/m which exerts magnetic force of 0.3 N on the at height of 5 cm, as shown in Fig. 4.5(b)

We allow a participant to explore the virtual flat surface without any prior information pertaining to the geometry of the object. They are asked to differentiate the virtual flat surface from other objects. During interaction the position of the wearable finger splint is measured and feedback to the haptic rendering algorithm to calculate the magnetic forces. The required constraint force at each of these points is then calculated, as shown in Fig. 4.5(b). In this representative trial, the maximum deviation between the wearable finger splint and the reference surface is 14 mm (at time $t \approx 1$ seconds). At time $t \approx 6$ seconds, the participant moves outside the workspace of the system, and this action is repeated by each participant to differentiate between 3D objects. Fig. 4.5(c) shows the input currents to the electromagnetic coils in this representative trial. These currents are calculated using the current control algorithm minimizes the error between the required surface constraint force of the virtual object and the controlled magnetic forces. The successful participants take 92 seconds to differentiate the virtual flat surface from other objects.

4.2.2 Magnetic Rendering of a Virtual Hemisphere

A virtual hemisphere with diameter of 100 mm is rendered, as shown in Fig. 4.6(a). The surface constraint is discretized into 3721 points. A constraint force at each of these points is calculated using (10) with a force constant λ of 6 N/m (0.3 N at height of 5 cm), as shown in Fig. 4.6(b). The input currents to the electromagnetic coils in this trial are shown in Fig. 4.6(c). Fig. 4.6(d) shows that the participant slides his finger and explore a virtual half-sphere in mid-air.

Our system enables rendering of one side (upperside) of the object only due to the planar configuration of the electromagnetic coils. Therefore, it is not possible to interact with the other side of the virtual object with the system in its current configuration. Nevertheless, it is possible to rotate the 3D object and recalculate the magnetic forces to allow the participant to fully interact with the virtual object

4.3 Participant Study and Statistical Analysis

We conduct a participant study to validate the ability of our electromagnetic-based haptic interface and the impedance-type haptic algorithm to render 3D virtual objects. Observations of ten participants with an average age of 23 are collected. Each participant is allowed to distinguish between four different 3D virtual objects, i.e., flat surface, half-sphere, half-cylinder, and wedge. The number of trials is limited to 16 trials for each participant and this experiment is repeated four times for each virtual object using our impedance-type haptic

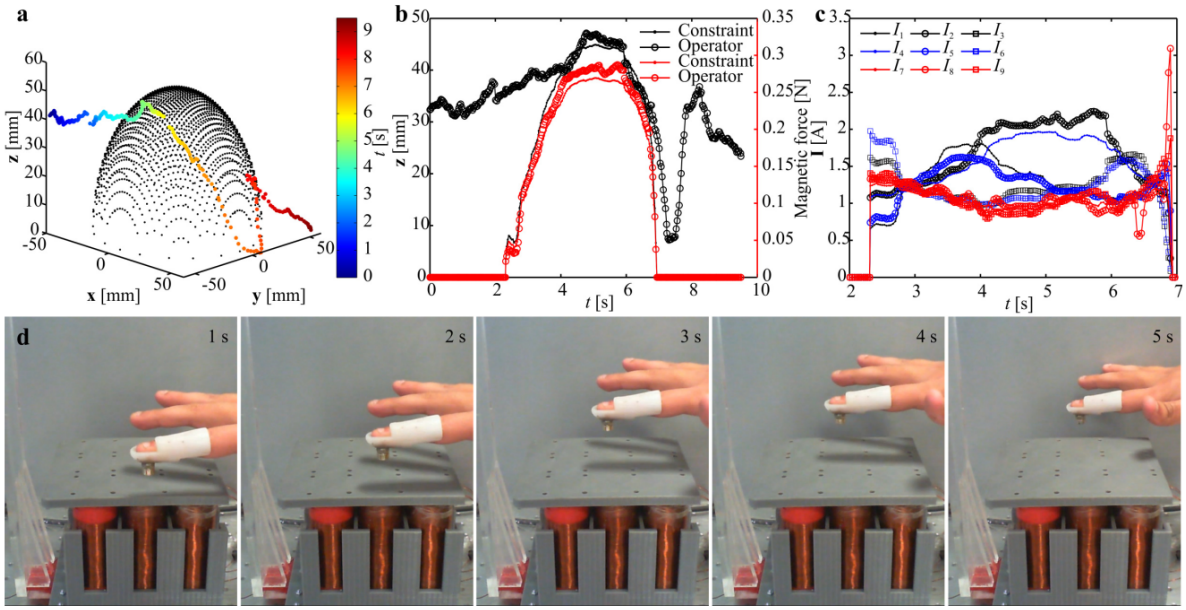

FIGURE 4.6: A representative magnetic rendering of a virtual half-sphere (with diameter of 100 mm) shows the position of the operator and the calculated forces and currents during shape differentiation. (a) The constraint surface of the flat surface is decomposed into 3721 points (small black circles). The trajectory of the finger splint indicates that the participant approaches towards the virtual sphere and move along its constraint surface. (b) Notable deviations between position of the participant along z-axis are observed only outside the virtual sphere owing to the absence of controlled magnetic forces. (c) Current inputs are calculated and supplied to the electromagnetic coils based on the position of the wearable finger split during this trial. (d) The participant slides his finger on the surface several times. The successful participants differentiate the virtual flat surface from other objects in 68 seconds.

algorithm (Case I) and in the absence of feedback (Case II). At the end of each trial, participants are asked to provide their observations. The result of each trial is not provided to the participant. Participants are allowed to spend some time training on the EHI before the experiment. All participants use the electromagnetic-based haptic interface for the first time and they are not involved again. In each trial, we measure the position of the finger during the interaction, exerted magnetic forces, and input currents to the electromagnetic coils, as shown in Fig. 4.5 and Fig. 4.6.

As a means to test the impedance-type magnetic haptic rendering algorithm (utilizes position feedback), ten participants are asked to differentiate between four virtual objects rendered using our EHI (flat surface, half-sphere, half-cylinder, and wedge). Participants wear a magnetic dipole attached to a finger splint which allows them to interact with the EHI as shown in Figure 3.6. Each shape is repeated four times in a random manner for a total of 16 trials for every participant. We apply no restrictions on the time spent by each participant to explore the virtual objects. Participants are advised to avoid fast horizontal movements (in the z-axes) in order to obtain the best experience. For each trial, we record the position of the finger, time spent during the interaction, and the current inputs to the EHI. Data from a total of 160 trials ($n = 160$) are used to build our observations.

Figure 4.7(a) shows the representative results of the impedance-type haptic algorithm for the mentioned four objects. We observe that participants differentiate between the objects

TABLE 4.1: EXPERIMENTAL RESULTS OF THE MAGNETIC RENDERING OF FOUR REPRESENTATIVE THREE-DIMENSIONAL (3D) VIRTUAL OBJECTS, I,E., FLAT SURFACE, HALF-SPHERE, HALF-CYLINDER, AND WEDGE. FIVE PARTICIPANTS EXPERIMENTALLY DEMONSTRATE $66.9 \pm 15.0\%$ SUCCESS RATE ($n = 160$) IN DISTINGUISHING THE FOUR 3D GEOMETRIES USING THE IMPEDANCE-TYPE HAPTIC RENDERING ALGORITHM. IN THE ABSENCE OF POSITION FEEDBACK, THE SUCCESS RATE IS $55.15 \pm 15.80\%$.

Object			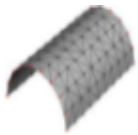	
Time (seconds)	**79.6 ± 47.3**	**64.9 ± 36.9**	**108.2 ± 62.0**	**64 ± 45**
Success Rate	**62.5%**	**67.5%**	**60%**	**77.5%**

in approximately 79 ± 21 ($n = 160$) seconds although the time of each trial is not limited. The successful and unsuccessful trials for each participant are shown in Fig. 4.7(a) using the filled and empty markers, respectively. Fig. 4.7(b) shows the average time taken by the ten participants for each object. For the virtual half-cylinder, participants spend 108.2 ± 62.0 ($n = 160$) seconds and achieve a success rate of 60 in their observations. The observation time is decreased to 79.6 ± 47.3 ($n = 160$) seconds for the virtual flat surface and the success rate is increased to 62.5. For the virtual sphere and wedge, the average observation time is measured as 64.9 ± 36.9 ($n = 160$) seconds and 64 ± 45($n = 160$) seconds with success rate of 67.5% and 77.5%, respectively. Therefore, the average success rate of the participants using the impedance-type haptic algorithm is 66.9 ± 14.40 ($n = 160$).

Although our impedance-type haptic algorithm is based on position feedback, it is also possible to explore a virtual object using static magnetic forces. These forces are calculated using (Equation 4.9) to minimize the force error (Equation 4.8) regardless of the position of the participant. We repeat the previous trials (differentiating between four virtual shapes) using the same participants in this case without position feedback. Table 4.2 shows the success rate of each of the ten participants in identifying the shape. Participants explored each shape in 4 of the 16 total trials in a random manner. Since each shape appears only in four trials, 1.0 indicates that the participant was able to successfully identify the shape in the 4 trials (100% success rate), 0.75 indicates that the participant was able to successfully identify the shape in 3 of the 4 trials (75% success rate). The success rate in distinguishing between the four virtual objects in the absence of position feedback is decreased to $55.15 \pm 15.80\%$ ($n = 160$) compared to $66.9 \pm 15.0\%$ ($n = 160$) success rate in case of utilizing position feedback (impedance type haptic rendering algorithm).

To understand the significance of position feedback in our system, we devise the following null (H_0) and alternative (H_a) hypothesis (confidence level of 90%):

- H_0: The success rate for Case I is less than that of Case II;
- H_a: The success rate for Case I is greater than that of Case II;

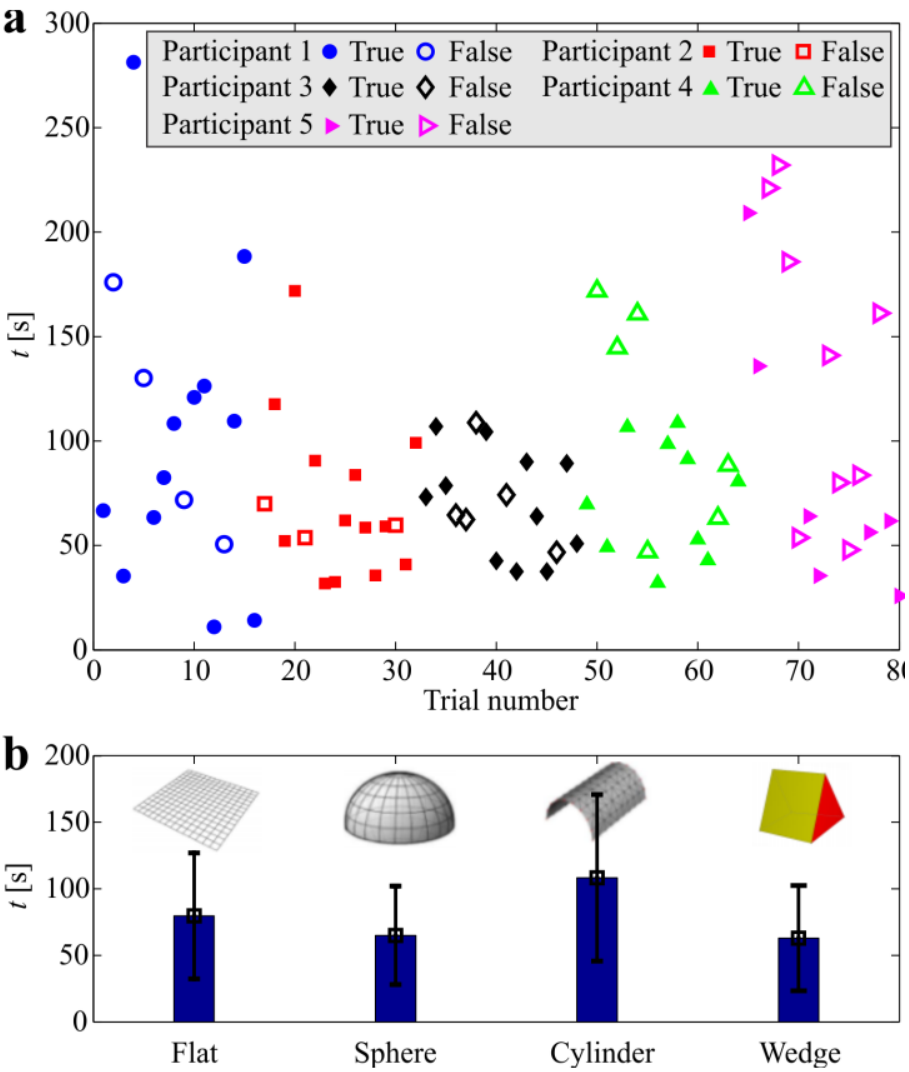

FIGURE 4.7: The observations of five representative participants indicate their ability to differentiate between four virtual shapes (flat, half-sphere, half-cylinder, and wedge). Each participant is allowed to distinguish between the objects for 16 trials only. Our system renders the objects in a random order and the result of each observation is not provided to the participant after each trial. (a) The filled and empty markers indicate the successful and unsuccessful trials, respectively. (b) Participants spent a relatively short time in making successful observations for the virtual sphere and wedge, as opposed to the virtual flat surface and half-cylinder.

Fig. 4.8(a) shows the number of successful trials for each participant in Case I (impedance-type haptic rendering) and Case II (rendering without position feedback). The observations are examined using the Paired T-test. First, we test the normality of the two groups of data using the Shapiro-Wilk test of normality. We conclude that the two groups of data are normally distributed. Second, the Paired T-Test suggests p-value $= 0.052 < \alpha$ Therefore, we reject the null hypothesis and accept the alternative hypothesis. Our experimental results show that participants achieve a success rate of 66.87% using the impedance-type rendering algorithm. This success rate is decreased to 55.15% for rendering 3D objects without position feedback. Our analysis shows that there is statistical evidence to conclude that the mean success rate for Case I is greater than that of Case II.The incorporation of position feedback has additional benefits such as the capability of rendering relatively complex virtual objects

TABLE 4.2: EXPERIMENTAL RESULTS OF THE MAGNETIC RENDERING OF FOUR REPRESENTATIVE THREE-DIMENSIONAL (3D) VIRTUAL OBJECTS, I.E. FLAT SURFACE, HALF-SPHERE, HALF-CYLINDER, AND WEDGE. FIVE PARTICIPANTS EXPERIMENTALLY DEMONSTRATE $66.87 \pm 15.0\%$ SUCCESS RATE ($n = 160$) IN DISTINGUISHING THE FOUR 3D GEOMETRIES USING THE IMPEDANCE-TYPE HAPTIC RENDERING ALGORITHM. IN THE ABSENCE OF POSITION FEEDBACK (BETWEEN BRACKETS), THE SUCCESS RATE IS $55.15 \pm 15.8\%$.

Object			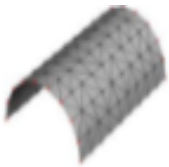	
1	**1.0 (0.75)**	**0.75 (0.5)**	**0.25 (0.5)**	**1.0 (1.0)**
2	**0.75 (0.5)**	**0.75 (0.5)**	**0.75 (0.75)**	**1.0 (1.0)**
3	**0.75 (0.75)**	**0.75 (0.75)**	**0.25 (0.25)**	**1.0 (0.75)**
4	**0.5 (0.75)**	**0.75 (0.75)**	**0.5 (0.25)**	**0.75 (0.5)**
5	**0.5 (0.5)**	**0.5 (0.0)**	**0.25 (0.0)**	**0.5 (0.75)**
6	**0.0 (0.75)**	**0.5 (1.0)**	**0.75 (0.5)**	**0.5 (0.5)**
7	**0.5 (0.75)**	**0.75 (0.75)**	**0.75 (0.75)**	**0.5 (0.75)**
8	**1.0 (0.75)**	**1.0 (0.5)**	**0.75 (0.5)**	**0.75 (0.25)**
9	**0.5 (0.5)**	**0.25 (0.5)**	**0.75 (0.25)**	**0.75 (0.25)**
10	**0.75 (0.25)**	**0.75 (0.25)**	**1.0 (0.75)**	**0.75 (0.25)**

and the utilization of lower current input owing to the activation of less number of coils based on the position of the wearable finger splint. However, the success rate is limited owing to the confusion between specific virtual objects during the experiments.

We construct the confusion matrix to show the predicted shapes (row) by the participants against the actual shapes (column) [Long et al., 2014b]. Table II shows the shapes that confuse the participants during the experiments while using our impedance-type rendering algorithm. Confusion between objects is observed in 15 trials between the flat surface and half-cylinder and in 13 trials between half-sphere and half-cylinder. Our measurements also show that the flat surface and half-sphere are confused in 11 trials, whereas the flat surface and wedge are confused in 10 trials. Table II shows that the participants are confused between the wedge and the half-sphere or the half-cylinder in 4 trials. In the absence of position feedback (observations between brackets), participants are confused most in differentiating between the virtual flat surface and the half-sphere in 12 trials, and the half-sphere and -cylinder in 16 trials. Participants are also confused between the flat surface and half-sphere

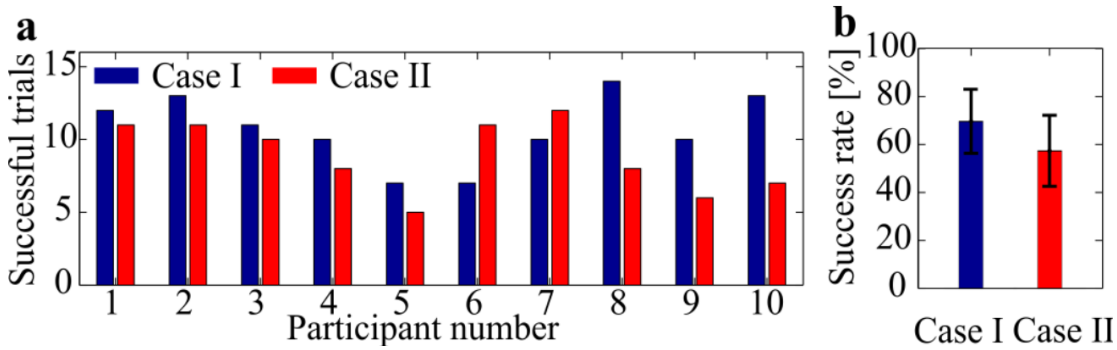

FIGURE 4.8: The ability of the participants to distinguish between the virtual geometries is enhanced by the incorporation of position feedback. (a) Measurements are collected from the observation of 10 participants using position feedback (Case I) and without (Case II) position feedback. (b) The impedance-type haptic interface enables participants to distinguish objects with 66.87% success rate, whereas exploring the virtual objects without position feedback achieves success rate of 55.15%. The means and standard deviations are calculated using 16 trials for each of the 10 participants in each case.

in 12 trials, and similarly, the virtual wedge and half-sphere and -cylinder are confused in 16 trials with all participants. Therefore, the incorporation of position feedback in the design of the impedance-type haptic algorithm decreases the confusion between virtual objects based on the observation of the participants.

4.4 Integration of Magnetic Rendering and Augmented Reality

The integration of magnetic rendering and augmented reality will enable contactless interaction with many objects that are not easy to access. A magnetic force can be wirelessly generated to render the boundaries of an object, whereas augmented reality will deploy its virtual image over other real-world objects. This combination is particularly promising for diagnosis and surgical simulation training. Currently, rigid phantoms and real patients are involved in surgical training. The former provides visual and geometry information regardless of the stiffness of a real organ, while the latter requires a relatively large number of patients with a wide range of diseased conditions. Therefore, the utilization of phantoms in diagnosis and surgical training does not enable the simulation of different conditions owing to their rigidity. This limitation can be been partially overcome by a wirelessly generated force in midair on a wearable haptic device. Rendering of virtual shapes using only haptic feedback without any visual feedback has demonstrated a small to moderate ability of participants to perceive the features of virtual objects owing to the following limitations: first, the magnitude of the force is inversely proportional to the distance to the magnetic field generation system and becomes lower than the sensory range of the operator for relatively large distances; second, the spatial resolution of the force is relatively low and limits the ability of the participants to differentiate between objects with similar features. Clearly, rendering virtual objects becomes more challenging in the absence of visual feedback.

The integration of magnetic rendering and augmented reality is demonstrated in Figure

TABLE 4.3: CONFUSION MATRIX SHOWS THE PREDICTED OBJECTS (ROW) VERSUS THE ACTUAL OBJECTS (COLUMN) FOR THE IMPEDANCE-TYPE HAPTIC INTERFACE ($n = 160$) AND FOR RENDERING VIRTUAL OBJECTS WITHOUT POSITION FEEDBACK ($n = 160$). MEASUREMENTS OF THE SECOND CASE IS SHOWN BETWEEN BRACKETS.

Object			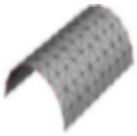	
	25 (24)	5 (4)	8 (15)	8 (5)
	6 (8)	**27 (22)**	7 (5)	0 (8)
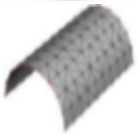	7 (6)	6 (11)	**24 (18)**	1 (3)
	2 (2)	2 (3)	1 (2)	**31 (24)**

4.9(a). Visual feedback is provided via a head-mounted display to deploy a virtual image (orange) over the real-world object (electromagnetic system), as shown in Figure 4.9(b). The orange model is programmed into the head-mounted display (Microsoft HoloLens, Microsoft Corporation Washington, U.S.A) and is positioned within the workspace of the electromagnetic system. The position and orientation of the participant's finger are measured and a controlled magnetic force is exerted to provide the boundaries of the virtual orange. Another virtual object (organ) is deployed over the electromagnetic system and its corresponding boundaries are rendered using magnetic forces to combine the visualization with the sense of touch. The integrated haptic AR interface is composed of the following subsystems: (1) an array of electromagnetic coils; (2) a wearable orthopedic finger splint with a magnetic dipole; (3) a head-mounted display; (4) position sensing device; (5) optimization and control algorithms. The operator combines visual and force feedback to explore the virtual object and interact with its boundaries.

An Augmented Reality scene is created to demonstrate the feasibility of incorporating magnetic haptic rendering in virtual environments. The scene created (Fig. 4.9(b,c)) includes a simple virtual orange placed on the surface of the EHI. The user is asked to explore and interact with the boundaries of the virtual orange in mid-air. The graphics of the scene are created using Blender computer graphics software. The virtual model is programmed to be placed on the EHI through hand gestures using Microsoft Visual Studio. The position and

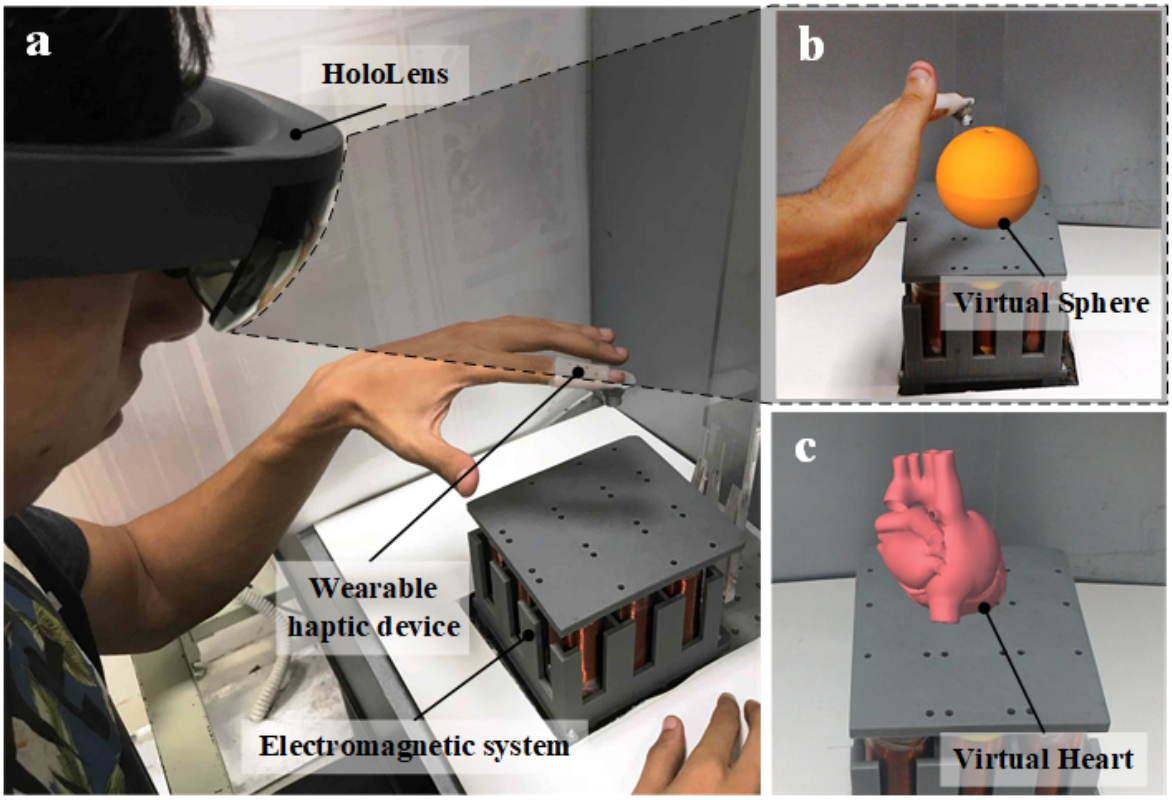

FIGURE 4.9: integration of magnetic rendering and AR enables a participant to interact with virtual objects. Visual feedback is provided via a head-mounted display. The constraint surface of the object is rendered using magnetic forces. These forces are exerted on a wearable orthopedic finger splint using an EHI. A virtual organ (heart) is deployed within the workspace of the electromagnetic system.

orientation of the participant's finger are measured using a position-sensing device (Leap Motion, San Francisco, CA, USA). When any collision with the virtual object is detected, the corresponding haptic feedback is activated.

4.5 Challenges and Discussions

The incorporation of position feedback into our control system enables a controlled magnetic force to be exerted on the wearable haptic device only when the participant slides his finger on the boundary of the virtual object. The resulting success rate is improved by 12% in shape differentiation owing to the nature of the position feedback-based closed-loop control system. Nevertheless, the ability of the participants to explore a 3D virtual object remains a challenge due to the limited projection distance of the magnetic force and the utilization of a single finger to explore the virtual environment. The first challenge places strong constraints on the size of the rendered virtual objects as the exerted force on the dipole of the wearable haptic device decays proportional to its distance to the coils cubed. The second challenge is in the design of the wearable haptic device. The current design is based on a single dipole

moment that simplifies the calculation of the magnetic force-current map (4) and the optimization routines. However, true interaction with the environment necessitates the utilization of all fingers and palm. Therefore, the wearable haptic device should be designed to provide multiple points of interaction to enhance the perception of the participants.

Our electromagnetic-based haptic interface represents a component of a wider human-computer interaction system that integrates magnetic rendering and augmented reality, as shown in Fig. 4.9(a). Fig. 4.9(b) shows a head-mounted display that visualizes the virtual environment, whereas the electromagnetic system enables the participant to explore its features and stiffness. Therefore, this system provides a human-computer interaction platform that offers promise for a variety of applications such as medical simulation training, minimally invasive surgery, and medical diagnosis systems. However, several challenges have to be overcome to develop surgical training systems based on our integrated haptic AR interface. A position-tracking device is crucial in the magnetic rendering process and becomes more valuable when integrating augmented reality with magnetic haptic rendering. Utilizing an optical position sensing device has several limitations such as sensitivity to illumination and line of sight requirements. Keeping the tracked object within the sight of the camera limits the range of movement. To overcome these limitations a magnetic-based localization system is developed for the EHI to estimate the position operator's hand [Adel et al., 2019]. The second challenge is to exert magnetic forces on multiple dipoles attached to the palm and all fingers to enhance the perception of the participants during interactions with the virtual objects. Currently, our system relies on a single dipole attached to an orthopedic finger splint. The operator wears a finger split with one dipole to interact with the virtual object via a single point of contact. Therefore, perception is likely to be enhanced for multiple points of interaction.

It is also necessary to measure the magnetic forces during rendering, hence incorporating force sensors within the orthopedic finger splint such that stiffness or impedance control can be implemented. Another challenge is to magnetically render and deploy deformable objects in real-time, and achieve stiffness control based on the elastic properties of the object. However, simultaneous visualization and interaction with deformable bodies require higher computational power and efficient optimization techniques during the control inputs calculation. The current configuration of the electromagnetic coils does not enable magnetic rendering of the complete object. Only the upper side of the object is rendered, and hence limits the ability of the operator to sense important features at the lower side. This problem can be solved by rendering objects using an omnidirectional electromagnet instead of coils with planar configuration, [Petruska and Abbott, 2013]. In this case, the omnidirectional electromagnet will be located at the center of the 3D virtual object, and magnetic forces will be exerted within a spherical workspace. Despite these challenges, our system provides a proof-of-concept for an efficient method to develop surgical training and diagnosis systems and represents a component of a wider human-computer interaction platform.

Chapter 5

Conclusions and Future Work

5.1 Conclusions

An electromagnetic-based haptic interface is designed, developed, and verified using observations of participants. A model of the magnetic forces exerted on a permanent magnet attached to a wearable finger splint is developed. This model serves as the foundation for optimizing the design of the electromagnetic coils, with the aim of providing a magnetic force of 2 N at a height of 3 cm. This system is based on an impedance-type haptic rendering algorithm that provides controlled magnetic force, enabling participants to perceive 3D virtual objects in mid-air. Furthermore, a magnetic localization system has been developed and experimentally validated for this electromagnetic haptic interface. This localization system capitalizes on the magnetic symmetry of the EHI for the elimination of its magnetic field, thereby obviating the need for a pre-calculated magnetic field map. The proposed system is validated under four different cases of the magnetic field generated by the EHI (zero, fixed, time-varying, and random). The magnetic tracking system validation experimental results show that the MAE in position estimation is 1.01 ± 0.45 mm ($n = 375$). In addition, our analysis also shows statistical evidence to conclude that the repeatability of our system is acceptable regardless of the magnetic field generated by the EHI, at 95% confidence level. The system's efficacy in rendering 3D virtual objects has been assessed both in the presence and absence of positional feedback, ten participants are asked to differentiate between four shapes (flat surface, half-sphere, half-cylinder, and wedge). The experimental results show that participants distinguish between the geometry of four 3D objects with a success rate of 66.87% while using position feedback (Case I) and 55.15% in the absence of position feedback(Case II). Statistical analysis shows evidence to conclude that the mean success rate for Case I is greater than that of Case II.

5.2 Future Work

As part of future studies, we will adapt our impedance-type rendering algorithm to incorporate multiple dipole moments to improve the perception of the participants during the interaction with virtual objects. The success rate of our system is limited to 66.87% owing to the dependence of our rendering algorithm on a single magnetic force. The incorporation of multiple magnetic dipoles will enable us to exert several controlled magnetic forces on specific locations within a wearable haptic device, and as a consequence, the success rate

in object differentiation will be improved. In addition, a head-mounted display will be integrated into our electromagnetic-based haptic interface to deploy virtual images of the 3D object over other real-world objects.

Appendix A

Background

A.1 Magnetostatics

A.1.1 Maxwell's Equations

Maxwell's equations group represent the foundation of classical electromagnetic theory in the mid-nineteenth century. They explain how magnetic field and the electric field in a given medium are coupled in time and space. Moreover, these equation represent constraints on the magnetic fields that we can generate using our electromagnetic-based haptic devices. Maxwell equations are written in the vectorial form as:

$$\nabla \times \mathbf{H} = \mathbf{J} + \frac{\partial \mathbf{D}}{\partial t}, \tag{A.1}$$

$$\nabla \times \mathbf{E} = -\frac{\partial \mathbf{B}}{\partial t}, \tag{A.2}$$

$$\nabla \cdot \mathbf{B} = 0, \tag{A.3}$$

$$\nabla \cdot \mathbf{D} = \rho_{\mathrm{e}}, \tag{A.4}$$

where H is the magnetic field intensity [Am^{-1}], B is the magnetic flux density [T]. D is the electric flux density [Cm^{-2}], E is the electric field intensity [Vm^{-1}] and J is the free current density [Am^{-2}]. ρ_{e} is the volume density of free electric charges [Cm^{-3}] and ∇ defines curl operation. These equations were not written at that compact form at the time maxwell began his work. The equations were known as the laws of Ampere-Maxwell (equation 2.1), Faraday (equation 2.2), Gauss-Faraday (equation 2.3), and Gauss (equation 2.4). The magnetic field vector and all its derivatives are assumed to be continuous at any point in the space such that,

$$\nabla \cdot \mathbf{J} + \frac{\partial \rho_{\mathrm{e}}}{\partial t} = 0 \tag{A.5}$$

where J is the source of the electromagnetic field and this relationship is known as the current conservation equation.

A.1.2 Magnetostatics

Magnetostatics refer to static magnetic fields, where the current is considered as static or quasi-static. A magneto-quasi-static field is typically generated by low-frequency induction from a magnetic dipole or a current loop and by neglecting either the magnetic induction or the electric displacement current Haus and Melcher, 1989. Quasi-static (near field) region simplifications requires that the wavelength λ of the electromagnetic field would be much greater than the dimension l of the conductor ($\lambda \gg l$). Appropriate quasi-static simplifications the Ampere's law (equation 2.1) is applied,

$$\nabla \times \mathbf{H} = \mathbf{J}, \tag{A.6}$$

where $\mathbf{B} = \mu\mathbf{H}$ and $\mu = \mu_0\mu_\mathrm{R}$ is the magnetic permeability, μ_0 is the permeability of free space $\mu_0 = 4\pi \times 10^{-7}[\mathrm{Hm}^{-1}]$. It is the measure of the ability of a material to resist the formation of a magnetic field. Materials with high permeabilities such as iron and the other ferromagnetic materials are more transparent to magnetic field lines than others. Other materials, such as plastics, wood, and air, have much lower permeabilities around zero. Given these simplifications, one of the pertinent equations tells us that, in general [Abbott, Diller, and Petruska, 2020]

$$\nabla \cdot \mathbf{B} = 0 \quad \Longrightarrow \quad \frac{\partial B_x}{\partial x} + \frac{\partial B_y}{\partial y} + \frac{\partial B_z}{\partial z} = 0, \tag{A.7}$$

where $\mathbf{B}$ is the magnetic-vector field and B_x, B_y and B_z are the components of the external magnetic field along x-,y-and z-axis, respectively. We assume that there is no electric current flowing through the rendering workspace. Maxwell equations provide a constraint on the curl of $\mathbf{B}$ at a given point in space based on the electric current flowing through that point and the time derivative in the electric field at that point,

$$\nabla \times \mathbf{B} = 0 \quad \Longrightarrow \quad \frac{\partial B_z}{\partial y} = \frac{\partial B_y}{\partial z}, \quad \frac{\partial B_x}{\partial z} = \frac{\partial B_z}{\partial x}, \quad \frac{\partial B_y}{\partial x} = \frac{\partial B_x}{\partial y}. \tag{A.8}$$

A.2 Magnetic Field calculation

A.2.1 Magnetic Field off the Symmetry Axis of a Current Loop

To find the magnetic field generated from an electromagnetic coil at a point $P(x, y, z)$, we start by calculating the magnetic field due to a circular loop of radius (R) lying in the xy plane and carrying a steady current (I). The magnetic field contribution from an infinitesimal current element $(I\mathbf{ds})$ of a circular loop can be computed using **Biot-Savart law**

$$d\mathbf{B} = \frac{\mu_0 I}{4\pi} \frac{d\mathbf{s} \times \mathbf{r}}{R^3} \tag{A.9}$$

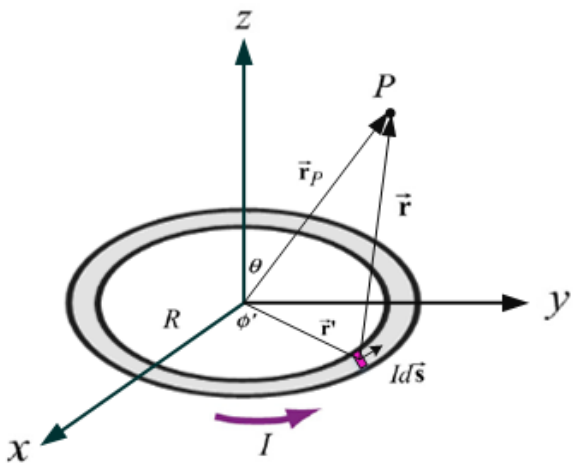

In Cartesian coordinates the differential current element of a circular current loop lying in the xy plane ($I\mathbf{ds}$) located at ($\mathbf{r}'$) can be written as

$$I\mathbf{ds} = I\frac{\mathbf{r}'}{d\phi'}d\phi' = Rd\phi'(-\sin\phi'\hat{\mathbf{i}} + \cos\phi'\hat{\mathbf{j}}) \qquad ; \qquad \mathbf{r}' = R(\cos\phi'\hat{\mathbf{i}} + \sin\phi'\hat{\mathbf{j}})$$

The spatial field point (P) with $\mathbf{r_p} = x\hat{\mathbf{i}} + y\hat{\mathbf{j}} + z\hat{\mathbf{k}}$. The corresponding relative position vector ($\mathbf{r}$) is given by

$$\mathbf{r} = \mathbf{r_p} - \mathbf{r}' = (x - R\cos\phi')\hat{\mathbf{i}} + (y - R\sin\phi')\hat{\mathbf{j}} + z\hat{\mathbf{k}}$$

Using the Biot-Savart law, the contribution of the current element to the magnetic field at P

$$d\mathbf{B} = \frac{\mu_0 I}{4\pi}\frac{d\mathbf{s}\times\mathbf{r}}{|\mathbf{r}|^3} = \frac{\mu_0 I}{4\pi}\frac{[Rd\phi'(-\sin\phi'\hat{\mathbf{i}} + \cos\phi'\hat{\mathbf{j}})]\times[(x - R\cos\phi')\hat{\mathbf{i}} + (y - R\sin\phi')\hat{\mathbf{j}} + z\hat{\mathbf{k}}]}{(\sqrt{R^2 + x^2 + y^2 + z^2 - 2Rx\cos\phi' - 2Ry\sin\phi'})^3}d\phi'$$

$$d\mathbf{B} = \frac{\mu_0 I}{4\pi}\frac{Rd\phi'(z\cos\phi'\hat{\mathbf{i}} + z\sin\phi'\hat{\mathbf{j}} + (R - x\cos\phi' - y\sin\phi')\hat{\mathbf{k}}}{(R^2 + x^2 + y^2 + z^2 - 2Rx\cos\phi' - 2Ry\sin\phi')^{3/2}}d\phi'$$

The magnetic field ($\mathbf{B} \in \mathbb{R}^3$) due to a circular current loop at the point ($P \in \mathbb{R}^3$) is

$$\mathbf{B} = \frac{\mu_0 RI}{4\pi}\int_0^{2\pi}\frac{z\cos\phi'\hat{\mathbf{i}} + z\sin\phi'\hat{\mathbf{j}} + (R - x\cos\phi' - y\sin\phi')\hat{\mathbf{k}}}{(R^2 + x^2 + y^2 + z^2 - 2Rx\cos\phi' - 2Ry\sin\phi')^{3/2}}d\phi'$$

then the x,y, and z components of the magnetic field can be written as

$$B_x = \frac{\mu_0 RI}{4\pi}\int_0^{2\pi}\frac{z\cos\phi'}{(R^2 + x^2 + y^2 + z^2 - 2Rx\cos\phi' - 2Ry\sin\phi')^{3/2}}d\phi'$$

$$B_y = \frac{\mu_0 RI}{4\pi}\int_0^{2\pi}\frac{z\sin\phi'}{(R^2 + x^2 + y^2 + z^2 - 2Rx\cos\phi' - 2Ry\sin\phi')^{3/2}}d\phi'$$

$$B_z = \frac{\mu_0 RI}{4\pi}\int_0^{2\pi}\frac{R - x\cos\phi' - y\sin\phi'}{(R^2 + x^2 + y^2 + z^2 - 2Rx\cos\phi' - 2Ry\sin\phi')^{3/2}}d\phi'$$

where ϕ' is the variable of integration around the circular coil and is integrated around the full circle from 0 to 2π.

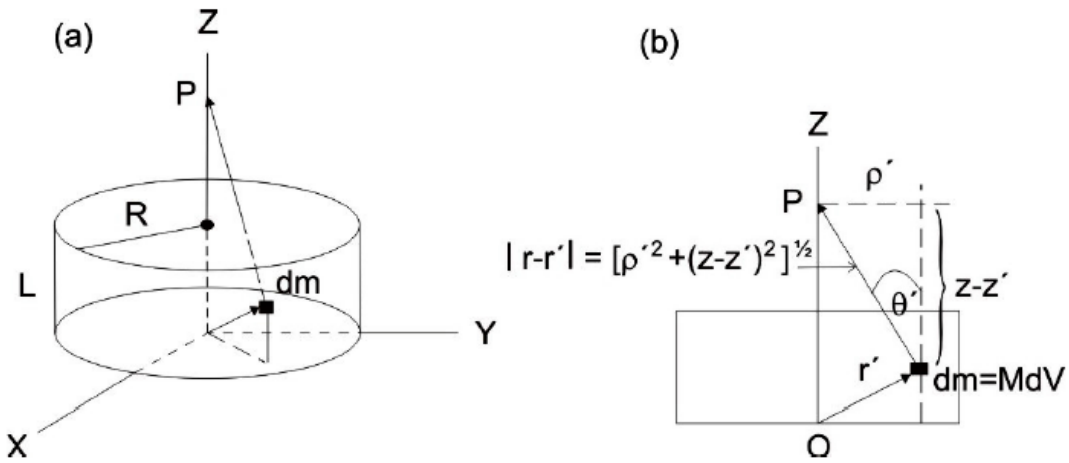

FIGURE A.1: Off-axis magnetic field generated by a cylindrical ferromagnetic core

A.2.2 Magnetic Field Due to Multi-layers Circular Turns Solenoid

To calculate the total magnetic field (B_x,B_y,B_z) from all turns of the solenoid equations can be integrated over the entire length of the solenoid (L) from ($-L/2$ to $L/2$). For a solenoid of outer radius (R_o) and inner radius (R_i), the total magnetic field due to the all layers can be calculated by further integrating over the layers' length from (R_i to R_o)

$$B_x = \frac{\mu_0 R I}{4\pi} \int_0^{2\pi} \int_{-L/2}^{L/2} \int_{R_i}^{R_o} \frac{z \cos\phi'}{(R^2 + x^2 + y^2 + z^2 - 2Rx\cos\phi' - 2Ry\sin\phi')^{3/2}} d\phi'$$

$$B_y = \frac{\mu_0 R I}{4\pi} \int_0^{2\pi} \int_{-L/2}^{L/2} \int_{R_i}^{R_o} \frac{z \sin\phi'}{(R^2 + x^2 + y^2 + z^2 - 2Rx\cos\phi' - 2Ry\sin\phi')^{3/2}} d\phi'$$

$$B_z = \frac{\mu_0 R I}{4\pi} \int_0^{2\pi} \int_{-L/2}^{L/2} \int_{R_i}^{R_o} \frac{R - x\cos\phi' - y\sin\phi'}{(R^2 + x^2 + y^2 + z^2 - 2Rx\cos\phi' - 2Ry\sin\phi')^{3/2}} d\phi'$$

these integrals can be written in terms of incomplete elliptic integrals of the first and second kind to be solved numerically.

A.2.3 Magnetic Field Due to a Cylindrical Ferromagnetic Core

The off-axis magnetic field generated by a ferromagnetic core ($\mathbf{B_c}$) placed in a nearly uniform magnetic field:

$$\mathbf{B_c} = -\mu_o \nabla \Phi$$

As you can see in the figure A.1 Assuming that the magnetized core is a continuous distribution of dipoles, which occupy a volume (dV) and have a magnetic dipole moment $d\mathbf{m} = \mathbf{M}dV$. The scalar potential of the field Φ is given by:

$$\Phi_{(x,y,z)} = \frac{M}{4\pi} \int_0^L \int_0^R \int_0^{2\pi} \frac{z - \grave{z}}{((r - \grave{r})^2 + R^2)^{1.5}} R dR dz d\phi$$

where R and L are the radius and the length of core respectively, $(r - \grave{r})^2 = (x - \grave{x})^2 + (y - \grave{y})^2 + (z - \grave{z})^2$ and M is the magnetization of core. We can calculate the magnetization (M) of the core by

$$M = \frac{B_0 \left(\mu_r - 1\right)}{\mu_o \left(1 + N \left(\mu_r - 1\right)\right)}$$

where B_0 is the applied magnetic field at the center of the core, r is the relative permeability of the core and N is the demagnetizing factor of the cylinder.

Bibliography

Abbott, Jake J., Eric Diller, and Andrew J. Petruska (2020). "Magnetic Methods in Robotics". In: *Annual Review of Control, Robotics, and Autonomous Systems* 3.1, null. DOI: 10.1146/annurev-control-081219-082713. eprint: https://doi.org/10.1146/annurev-control-081219-082713. URL: https://doi.org/10.1146/annurev-control-081219-082713.

Adel, A. et al. (2018). "Rendering of Virtual Volumetric Shapes Using an Electromagnetic-Based Haptic Interface". In: *2018 IEEE/RSJ International Conference on Intelligent Robots and Systems (IROS)*, pp. 1–9.

Adel, A. et al. (2019). "Magnetic Localization for an Electromagnetic-Based Haptic Interface". In: *IEEE Magnetics Letters* 10, pp. 1–5. ISSN: 1949-3088.

Adel, Alaa et al. (2017). "Design and development of an electromagnetic-based haptic interface". In: *Proceedings of the IEEE International Conference on Intelligent Robots and Systems (IROS), Vancouver, BC, Canada*.

Arafsha, F. et al. (2015). "Contactless haptic feedback: state of the art". In: *2015 IEEE International Symposium on Haptic, Audio and Visual Environments and Games (HAVE)*, pp. 1–6.

Berkelman, P., M. Miyasaka, and J. Anderson (2012). "Co-located 3D graphic and haptic display using electromagnetic levitation". In: *2012 IEEE Haptics Symposium (HAPTICS)*, pp. 77–81.

Berkelman, Peter, Zack Butler, and Ralph Hollis (1996). "Design of a Hemispherical Magnetic Levitation Haptic Interface Device". In: *Proceedings of the ASME IMECE Haptic Symposium*. Vol. 58, pp. 483 –488.

Berkelman, Peter J., Sebastian Bozlee, and Muneaki Miyasaka (2013). "Interactive Dynamic Simulations with Co-Located Maglev Haptic and 3D Graphic Display". In: *ACHI 2013*.

Berkelman, Peter J. and Ralph L. Hollis (2000). "Lorentz Magnetic Levitation for Haptic Interaction: Device Design, Performance, and Integration with Physical Simulations". In: *The International Journal of Robotics Research* 19.7, pp. 644–667. DOI: 10.1177/027836490001900703. eprint: https://doi.org/10.1177/027836490001900703. URL: https://doi.org/10.1177/027836490001900703.

Bermejo, Carlos and Pan Hui (2017a). "A survey on haptic technologies for mobile augmented reality". In: *Computing Research Repository* abs/1709.00698. arXiv: 1709.00698.

— (2017b). "A survey on haptic technologies for mobile augmented reality". In: *ArXiv* abs/1709.00698.

Brink, J. B. et al. (2014). "Factors affecting the design of untethered magnetic haptic interfaces". In: *2014 IEEE Haptics Symposium (HAPTICS)*, pp. 107–114.

Coles, T. R., D. Meglan, and N. W. John (2011). "The Role of Haptics in Medical Training Simulators: A Survey of the State of the Art". In: *IEEE Transactions on Haptics* 4.1, pp. 51–66.

Cybenko, G. (1989). "Approximation by superpositions of a sigmoidal function". In: *Mathematics of Control, Signals and Systems* 24, pp. 303–314. DOI: https://doi.org/10.1007/BF02551274.

Escobar-Castillejos, David et al. (2016). "A Review of Simulators with Haptic Devices for Medical Training". In: *Journal of Medical Systems* 40, pp. 1–22.

Hannaford, Blake and Allison M. Okamura (2016). "Haptics". In: *Springer Handbook of Robotics*. Ed. by Bruno Siciliano and Oussama Khatib. Cham: Springer International Publishing, pp. 1063–1084. ISBN: 978-3-319-32552-1. DOI: 10.1007/978-3-319-32552-1_42. URL: https://doi.org/10.1007/978-3-319-32552-1_42.

Haus, Hermann A and James R Melcher (1989). *Electromagnetic fields and energy*. Vol. 107. Prentice Hall Englewood Cliffs, NJ.

Hoshi, T., D. Abe, and H. Shinoda (2009). "Adding tactile reaction to hologram". In: *RO-MAN 2009 - The 18th IEEE International Symposium on Robot and Human Interactive Communication*, pp. 7–11.

Hu, John et al. (2006). "Effectiveness of haptic feedback in open surgery simulation and training systems". In: *Stud. Health Technol. Inform* 119, pp. 213–218.

Iwamoto, Takayuki et al. (2008). "Airborne Ultrasound Tactile Display". In: *ACM SIGGRAPH 2008 New Tech Demos*. SIGGRAPH '08. Los Angeles, California: Association for Computing Machinery. ISBN: 9781450378475. DOI: 10.1145/1401615.1401616. URL: https://doi.org/10.1145/1401615.1401616.

Khalil, Islam S. M., Leon Abelmann, and Sarthak Misra (2014). "Magnetic-Based Motion Control of Paramagnetic Microparticles With Disturbance Compensation". In: *IEEE Transactions on Magnetics* 50.10, pp. 1–10. DOI: 10.1109/TMAG.2014.2323940.

Lee, Hojin et al. (2016). "LaserStroke: Mid-Air Tactile Experiences on Contours Using Indirect Laser Radiation". In: *Proceedings of the 29th Annual Symposium on User Interface Software and Technology*. UIST '16 Adjunct. Tokyo, Japan: Association for Computing Machinery, 73–74. ISBN: 9781450345316. DOI: 10.1145/2984751.2985708. URL: https://doi.org/10.1145/2984751.2985708.

Li, M. et al. (2014). "A novel tumor localization method using haptic palpation based on soft tissue probing data". In: *2014 IEEE International Conference on Robotics and Automation (ICRA)*, pp. 4188–4193.

Long, Benjamin et al. (Nov. 2014a). "Rendering Volumetric Haptic Shapes in Mid-Air Using Ultrasound". In: *ACM Trans. Graph.* 33.6. ISSN: 0730-0301. DOI: 10.1145/2661229.2661257. URL: https://doi.org/10.1145/2661229.2661257.

— (2014b). "Rendering Volumetric Haptic Shapes in Mid-Air Using Ultrasound". In: *ACM Trans. Graph.* 33.6. ISSN: 0730-0301. DOI: 10.1145/2661229.2661257. URL: https://doi.org/10.1145/2661229.2661257.

Martinez, J. et al. (2019). "Mid-Air Haptic Algorithms for Rendering 3D Shapes". In: *2019 IEEE International Symposium on Haptic, Audio and Visual Environments and Games (HAVE)*, pp. 1–6.

Ochiai, Yoichi et al. (2016). "Cross-Field Aerial Haptics: Rendering Haptic Feedback in Air with Light and Acoustic Fields". In: *Proceedings of the 2016 CHI Conference on Human Factors in Computing Systems*. CHI '16. San Jose, California, USA: Association for Computing Machinery, 3238–3247. ISBN: 9781450333627. DOI: 10.1145/2858036.2858489. URL: https://doi.org/10.1145/2858036.2858489.

Otaduy, Miguel A. and Ming C. Lin (2005). "Introduction to Haptic Rendering". In: *ACM SIGGRAPH 2005 Courses*. SIGGRAPH '05. Los Angeles, California: Association for Computing Machinery, p. 3. DOI: 10.1145/1198555.1198603. URL: https://doi.org/10.1145/1198555.1198603.

Palmerius, K. L. et al. (2011). "Ultrasound palpation by haptic elastography". In: *2011 24th International Symposium on Computer-Based Medical Systems (CBMS)*, pp. 1–6.

Petruska, A. J. and J. J. Abbott (2013). "An omnidirectional electromagnet for remote manipulation". In: *2013 IEEE International Conference on Robotics and Automation*, pp. 822–827.

Petruska, A. J. and B. J. Nelson (2015). "Minimum Bounds on the Number of Electromagnets Required for Remote Magnetic Manipulation". In: *IEEE Transactions on Robotics* 31.3, pp. 714–722. ISSN: 1941-0468. DOI: 10.1109/TRO.2015.2424051.

Salcudean, S. E. and T. D. Vlaar (Mar. 1997). "On the Emulation of Stiff Walls and Static Friction With a Magnetically Levitated Input/Output Device". In: *Journal of Dynamic Systems, Measurement, and Control* 119.1, pp. 127–132. ISSN: 0022-0434. DOI: 10.1115/1.2801204. eprint: https://asmedigitalcollection.asme.org/dynamicsystems/article-pdf/119/1/127/5540596/127_1.pdf. URL: https://doi.org/10.1115/1.2801204.

Sodhi, Rajinder et al. (July 2013). "AIREAL: Interactive Tactile Experiences in Free Air". In: *ACM Trans. Graph.* 32.4. ISSN: 0730-0301. DOI: 10.1145/2461912.2462007. URL: https://doi.org/10.1145/2461912.2462007.

Spelmezan, D., R. M. González, and S. Subramanian (2016). "SkinHaptics: Ultrasound focused in the hand creates tactile sensations". In: *2016 IEEE Haptics Symposium (HAPTICS)*, pp. 98–105.

Suzuki, Y. and M. Kobayashi (2005). "Air jet driven force feedback in virtual reality". In: *IEEE Computer Graphics and Applications* 25.1, pp. 44–47.

Tong, Q. et al. (2018). "Magnetic Levitation Haptic Augmentation for Virtual Tissue Stiffness Perception". In: *IEEE Transactions on Visualization and Computer Graphics* 24.12, pp. 3123–3136.

Ullrich, S. and T. Kuhlen (2012). "Haptic Palpation for Medical Simulation in Virtual Environments". In: *IEEE Transactions on Visualization and Computer Graphics* 18.4, pp. 617–625.

Zhang, Q., H. Dong, and A. El Saddik (2016). "Magnetic Field Control for Haptic Display: System Design and Simulation". In: *IEEE Access* 4, pp. 299–311.